

Report No. IITRI-A6155-5

COMPOSITIONAL ANALYSIS  
OF LUNAR AND PLANETARY SURFACES  
USING NEUTRON CAPTURE GAMMA RAYS

for

Dr. Martin J. Swetnick

Code SL

National Aeronautics and Space Administration  
Washington, D. C. 20546

Report No. IITRI-A6155-5

COMPOSITIONAL ANALYSIS  
OF LUNAR AND PLANETARY SURFACES  
USING NEUTRON CAPTURE GAMMA RAYS

May 1, 1966 to June 30, 1967

Prepared by

John H. Reed

of

IIT RESEARCH INSTITUTE  
Technology Center  
10 West 35th Street  
Chicago, Illinois 60616

for

Dr. Martin J. Swetnick  
Code SL  
National Aeronautics and Space Administration  
Washington, D. C. 20546

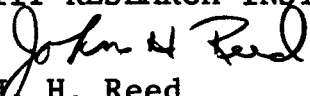
July 1, 1967

## FOREWORD


This is Report No. IITRI-A6155-5, an annual report under Contract No. NASr 65(18), entitled "Compositional Analysis of Lunar and Planetary Surfaces Using Neutron Capture Gamma Rays," covering the period May 1, 1966 to June 30, 1967.


The following personnel have contributed to the work described in this report: J. H. Reed, principal investigator, J. W. Mandler, D. T. Krebs and D. A. Klopp.

Respectfully submitted,  
IIT RESEARCH INSTITUTE

  
J. H. Reed  
Research Physicist

Approved:

  
R. B. Moler  
Manager  
Nuclear and Radiation Physics

  
F. L. Adelman  
Assistant Director  
Physics Division

/gw

## ABSTRACT

### COMPOSITIONAL ANALYSIS OF LUNAR AND PLANETARY SURFACES USING NEUTRON CAPTURE GAMMA RAYS

The objective of this research program is to establish the practicability of using neutron capture gamma rays as a part of NASA's combined neutron experiment for lunar and planetary surface analysis. To accomplish this task it is necessary first to determine the feasibility of the analysis of a semi-infinite material by means of the capture gamma-ray technique using a pulsed high-energy neutron source, secondly to assess the effect on sensitivity of integration with the other neutron techniques, and lastly, to determine the sensitivity of the technique under reasonable field conditions.

Computer calculations were performed using the one-dimensional DTK neutron transport computer code assuming an isotropic 14-MeV neutron source on the surface of a large sample, to help in understanding the effects of composition, density, hydrogen content, and partial moderators on the thermal flux distribution within the sample. The results predicted that, in the absence of a moderating material, the flux of thermal neutrons increases with depth and reaches a maximum at about  $90 \text{ gm/cm}^2$  below the surface of the sample. If a paraffin reflector a few centimeters in thickness is placed above the 14-MeV neutron source, however, the thermal flux at the surface is greatly increased, and, in fact, has its maximum value there. These computer predictions were verified experimentally by measuring the thermal flux distribution in a large sand sample both with and without a reflector above the 14-MeV neutron source.

A parametric study was made to determine the effects of such variables as the length of the sampling period, the neutron pulse rate, etc., on the sensitivity of the capture

gamma-ray technique. Results of this study have established the feasibility of applying the capture gamma-ray technique to the analysis of semi-infinite samples using a pulsed 14-MeV neutron source. In addition, it was determined that a good quality capture gamma-ray spectrum can be obtained under the following conditions: 1) horizontal detector-source geometry, with the detector located 27 cm from the source, 2) a 15-cm copper shadow shield located between the detector and the source, 3) an 8-cm paraffin reflector located above the source, 4) a 500-pps neutron pulse rate, and 5) one 250- $\mu$ sec sampling period after each neutron pulse (to obtain capture gamma-ray data) and an equal sampling period just before each neutron pulse (to obtain background data).

As a result of this study, then, it has been concluded that the capture gamma-ray technique is feasible with a pulsed source of high-energy neutrons and that certain constraints on the combined neutron experiment would increase the utility of this technique. Further study is required to establish the sensitivity of the capture gamma-ray technique in the combined experiment and to ascertain the compatibility of these constraints with the other experiments to be included.

## TABLE OF CONTENTS

	Page
FOREWORD	ii
ABSTRACT	iii
LIST OF FIGURES	vi
LIST OF TABLES	ix
I. INTRODUCTION	1
II. RADIATIVE CAPTURE OF THERMAL NEUTRONS	4
III. THE NEUTRON DISTRIBUTION WITHIN A SEMI-INFINITE MATERIAL	13
IV. PROCEDURE USED FOR OBTAINING CAPTURE GAMMA-RAY SPECTRA	28
V. PARAMETRIC STUDY	44
VI. REMAINING PROBLEM AREAS	69
REFERENCES	72
APPENDIX A OPTIMUM SAMPLING PERIOD	A-1
APPENDIX B ORIGIN OF THE CAPTURE AND INDUCED GAMMA RAYS	B-1
APPENDIX C SAMPLE OF DIGITAL DATA	C-1

## LIST OF FIGURES

Figure		Page
1	Capture Gamma-Ray Spectrum of Basalt Obtained Using NaI(Tl) Detector	7
2	Capture Gamma-Ray Spectrum of Basalt Obtained Using Ge(Li) Detector	8
3	Time Relationship of the Gamma Rays Present in the Combined Neutron Experiment	12
4	One-Dimensional Geometry Used for Computer Calculations	15
5	Experimental Geometry	16
6	The Effect of Gross Composition on the Thermal Neutron Flux Distribution	18
7	Thermal Neutron Flux Distribution as a Function of Hydrogen Concentration	20
8	Thermal Neutron Flux Distribution as a Function of Reflector Thickness	21
9	Contour Plot of the Thermal Flux Distribution in Sand Sample with 4 cm of Reflector Above the Neutron Source and Source 15 cm above the Sample	26
10	Schematic Diagram of the Preamplifier	32
11	Schematic Diagram of the Analyzer Sequence Switch	34
11a	Schematic Diagram of Flip Flop	35
11b	Schematic Diagram of One Shot	36
12	Block Diagram of the Data Collection System	37
13	Timing Diagram for Analyzer Sequence Switch	39
14	Capture Gamma-Ray Spectrum of Sand	41
15	Capture Gamma-Ray Spectrum of Silicon	42
16	Capture Gamma-Ray Spectrum of Iron	43

# LIST OF FIGURES (contd.)

Figure		Page
17	Capture Gamma-Ray Spectrum of Iron-Sand Sample Obtained Using No Paraffin Above Target	48
18	Capture Gamma-Ray Spectrum of Iron-Sand Sample Obtained Using 2 cm Paraffin Above Target	49
19	Capture Gamma-Ray Spectrum of Iron-Sand Sample Obtained Using 4 cm Paraffin Above Target	50
20	Capture Gamma-Ray Spectrum of Iron-Sand Sample Obtained Using 8 cm Paraffin Above Target	51
21	Experimental Configuration	54
22	Capture Gamma-Ray Spectrum of Iron-Sand Sample Obtained Using Horizontal Geometry With 37 cm Target to Crystal Distance	56
23	Capture Gamma-Ray Spectrum of Iron-Sand Sample Obtained Using Horizontal Geometry With 52 cm Target to Crystal Distance	57
24	Capture Gamma-Ray Spectrum of Iron-Sand Sample Obtained Using Vertical Geometry With 32 cm Target to Crystal Distance	58
25	Capture Gamma-Ray Spectrum of Iron-Sand Sample Obtained Using Vertical Geometry With 47 cm Target to Crystal Distance	59
26	Capture Gamma-Ray Spectrum of Iron-Sand Sample Obtained Using 4 in. of Lead Between Target and Shadow Shield	61
27	Capture Gamma-Ray Spectrum of Iron-Sand Sample Obtained Using SANDIA Geometry With 4 cm Paraffin Above Target	62

# LIST OF FIGURES (contd.)

Figure		Page
28	Capture Gamma-Ray Spectrum of Iron-Sand Sample Obtained Using SANDIA Geometry With 8 cm Paraffin Above Target	63
29	Capture Gamma-Ray Spectrum of Iron-Sand Sample Obtained Using SANDIA Geometry With 4 cm Boronated Paraffin Above Target	65
30	Capture Gamma-Ray Spectrum at Iron-Sand Sample Obtained Using SANDIA Geometry With 4 cm Paraffin Above Target and 1000 pps Pulse Rate	66
A-1	Optimum Sample Duration as a Function of $N_0/B$	A-3
B-1	The Relative Location of Zone S and Zone D	B-4
B-2	Contour Plot of the Thermal Neutron Flux Distribution in Iron-Sand Sample with 4 cm of Reflector Above the Neutron Source and Source 5 cm Above the Sample	B-7

# LIST OF TABLES

	Page
1. Relative "Sensitivities" for Detection of Elements in Common Rocks Using Thermal Neutron Capture Gamma Rays	5
2. Assumed Sample Compositions for Computer Calculations	17
3. Thermal Flux Distribution in Sand Sample Without Paraffin Above the Source	24
4. Thermal Flux Distribution in Sand Sample With Paraffin Above the Source	27
5. Relative Efficiencies of Shields for Neutron Shielding of the Crystal	30
6. The Effect of Reflector Thickness (Above the Neutron Source) on Spectral Response	47
7. The Effect of Moderator Thickness (Between the Target and Sample) on Spectral Response	52
8. The Effect of Detector Position on Spectral Response (500 pps Pulse Rate)	55
B-1 Origin of Gamma Rays Reaching the Detector with Source 5 cm Above Surface	B-9

## CHAPTER I

### INTRODUCTION

One of the objectives of the space program is to ascertain the composition of lunar and planetary surfaces. Such information is of great importance to those in the scientific community who are concerned with the origin and the evolution of the moon and planets. Unfortunately, it does not appear that a significant number of samples will be returned from the moon for detailed analysis in the foreseeable future, and none will be available from the planets. Therefore, remote analysis of these surfaces is required. It is for this reason that NASA is presently developing a combined neutron experiment<sup>(1)</sup> for compositional analysis.

Four different neutron analytical methods (inelastic neutron scattering, capture gamma-ray analysis, activation analysis, and thermal neutron die-away) are being integrated into a single package, each of which is to utilize the same gamma-ray detector, 14-MeV pulsed neutron source, and the same multichannel pulse height analyzer. The four methods differ in the neutron properties utilized. Prompt gamma rays result from the inelastic scattering of fast neutrons and have discrete energies characteristic of the scattering nuclei. Capture gamma rays arise from the decay of excited energy levels of a compound nucleus after the capture of a neutron by a parent nucleus. The capture radiation is characteristic of the compound nucleus. Activation gamma rays are associated with the beta decay of radioactive nuclei produced by either fast neutron reactions or thermal neutron capture. The lifetime that the thermal neutrons exhibit in a semi-infinite sample (die-away) is a measure of the macroscopic neutron absorption cross section, which is a function of the material composition and density.

Three of these methods (inelastic scattering, capture gamma rays, and activation analysis) can provide elemental analysis; two of the methods (capture gamma ray and neutron die-away) can determine the presence of hydrogen, and one of the techniques (neutron die-away) can give some indication of the presence or absence of near-surface layering. Thus, the combined neutron experiment will provide information on both elemental composition and density.

The present report is concerned with the results of feasibility studies on the capture gamma-ray portion of the combined experiment. Measurements of the capture gamma-ray spectrum from a large iron-sand sample have been made under varying conditions using a pulsed 14-MeV neutron source and a 3 in. x 3 in. NaI(Tl) gamma-ray detector. As a result of these studies the following tentative conclusions have been reached:

- 1) The feasibility of the analysis of a semi-infinite material by means of the capture gamma-ray technique has been established using a pulsed 14-MeV neutron source.

- 2) The capture gamma-ray experiment can provide an analysis in the form of relative elemental abundances. Since only a sample containing iron, silicon, and oxygen has been examined thus far by this technique, the number of elements that can be measured is as yet undetermined.

- 3) The oxygen-silicon ratio can be established by cyclic activation. When more complex samples are examined, other elements (such as Al or Mg) may also be detectable.

- 4) The capture gamma-ray technique is sensitive to the material composition to a depth of 10 to 20 gm/cm<sup>2</sup>.

- 5) The compatibility of the four experiments has not yet been firmly established. However, we are confident that, with reasonable trade-offs, the capture gamma-ray experiment can be made compatible with the other experiments.

In Chapter II the application of radiative capture of thermal neutrons to elemental analysis is discussed, as well as those areas that will require investigation if the technique is to be applied to semi-infinite samples with the aid of pulsed 14-MeV neutron sources.

In Chapter III the thermal neutron distribution that results within a semi-infinite material when a high energy neutron source is placed on the surface of the material is described. This thermal neutron distribution was determined both experimentally and by a one-dimensional neutron transport calculation.

Chapter IV is a description of the equipment and procedures that have been used in the capture gamma-ray experimentation.

Chapter V contains a detailed account of the studies that have been made to determine the effect of various experimental parameters on the sensitivity of the capture gamma-ray technique.

In Chapter VI the major areas that require further study to establish the sensitivity of the capture gamma-ray technique and the feasibility of the combined neutron experiment are outlined.

## CHAPTER II

### THERMAL NEUTRON CAPTURE GAMMA-RAY ANALYSIS

For most elements, the  $(n, \gamma)$  reaction is the only nuclear reaction which can occur when a sample is irradiated with thermal neutrons. (A few light elements in which alpha particle or proton emission can occur and the fissionable isotopes are exceptions.) Neutron capture leads to the formation of a compound nucleus in an excited state, with an excitation energy essentially equal to the neutron binding energy (usually 5 to 8 MeV). Decay to the ground state occurs promptly (within approximately  $10^{-14}$  seconds), normally through several intermediate energy states, by gamma-ray emission. As a result of this decay through the intermediate states, neutron capture gamma-ray spectra are, in general, complex. These spectra, which are characteristic of the emitting isotope, will consist of both high and low energy gamma rays.

For a thin sample, that is, for a sample which transmits neutrons with little or no attenuation, capture gamma-ray production is directly proportional to the total neutron capture cross section of the sample. In a sample containing several elements, the quantity  $\sigma/A$  for each element (where  $\sigma$  is the thermal neutron capture cross section for a particular element and  $A$  is its atomic weight) provides an indicator of the relative sensitivities (measured in units of weight percent) for measurement of those elements using a neutron capture gamma-ray technique. Table 1 shows values of weight percent multiplied by  $\sigma/A$  for the elements occurring in granite, andesites, basalt, and dunite. It must be emphasized that the product (Wt percent)( $\sigma/A$ ) does not take into account branching ratios, detection efficiencies, interferences, or other effects, and is, therefore, an indicator only of the relative numbers of neutrons captured by each element in the sample.

Table 1  
RELATIVE "SENSITIVITIES" FOR DETECTION OF ELEMENTS IN TYPICAL SAMPLES OF  
COMMON ROCKS USING THERMAL NEUTRON CAPTURE GAMMA RAYS

Element	Granite		Andesites		Basalt		Dunite	
	Wt%*	(Wt%)( $\sigma/A$ )	Wt%*	(Wt%)( $\sigma/A$ )	Wt%*	(Wt%)( $\sigma/A$ )	Wt%*	(Wt%)( $\sigma/A$ )
H	0.09	0.030	0.14	0.047	0.18	0.060	0.32	0.11
Si	32.75	0.19	27.81	0.16	22.90	0.13	18.90	0.11
Fe	2.44	0.12	4.67	0.22	8.58	0.40	6.22	0.29
Al	7.23	0.061	8.65	0.074	7.85	0.067	0.43	0.0036
Mg	0.53	0.0015	1.66	0.0048	3.72	0.011	27.94	0.081
Na	2.58	0.052	2.66	0.053	2.31	0.046	0.07	0.0014
Ca	1.42	0.016	4.15	0.046	6.40	0.070	0.50	0.0055
K	3.41	0.18	1.69	0.089	1.26	0.067	0.03	0.0016
Mn	0.09	0.022	0.14	0.034	0.23	0.055	0.12	0.029
Ti	0.23	0.028	0.46	0.055	0.82	0.098	0.01	0.0012
O	45.7	0	47.8	0	45.5	0	45.4	0

\*Average composition as reported by T. F. W. Barth, Theoretical Petrology,  
John Wiley and Sons

## Laboratory Use of Capture Gamma-Ray Analysis With Thermal Neutrons

It would be instructive to perform a capture gamma-ray analysis in the laboratory on a sample which is similar to lunar material. At this time, however, the only existing data regarding the type of material to be encountered on the moon are the gamma-ray spectral measurements made by the Soviet lunar orbiter, "Luna 10".

A. P. Vinogradov et al.<sup>(2)</sup> report that the potassium, thorium, and uranium concentrations in those regions of the lunar surface where measurements were made are close to the composition of terrestrial rocks of basic composition (such as basalt). Vinogradov does not exclude, however, the possibility of the existence of ultrabasic (meteorite) matter for these regions of the lunar surface. If one assumes that the lunar surface has the composition of basalt, the elements one would expect to detect, in order of decreasing "sensitivity" as indicated in Table 1 would be iron, silicon, titanium, calcium, aluminum, potassium, hydrogen, manganese, sodium, and magnesium. The capture gamma-ray spectrum of basalt obtained from a beam of thermal neutrons from a reactor incident on a small sample of basalt, using a 3 in. x 3 in. NaI(Tl) detector, is shown in Figure 1. Iron, silicon, hydrogen, titanium, and possibly also aluminum, sodium, and calcium are detectable.

To demonstrate the improved results attainable using presently available Ge(Li) detectors of much better resolution ( $\sim 3$  keV FWHM) and small volume ( $1 \text{ cm}^3$ ), the comparison spectrum shown in Figure 2 was obtained. This basalt spectrum taken with a Ge(Li) detector provides the data necessary to obtain the relative concentrations of all the elements listed in Table 1 except magnesium and oxygen.

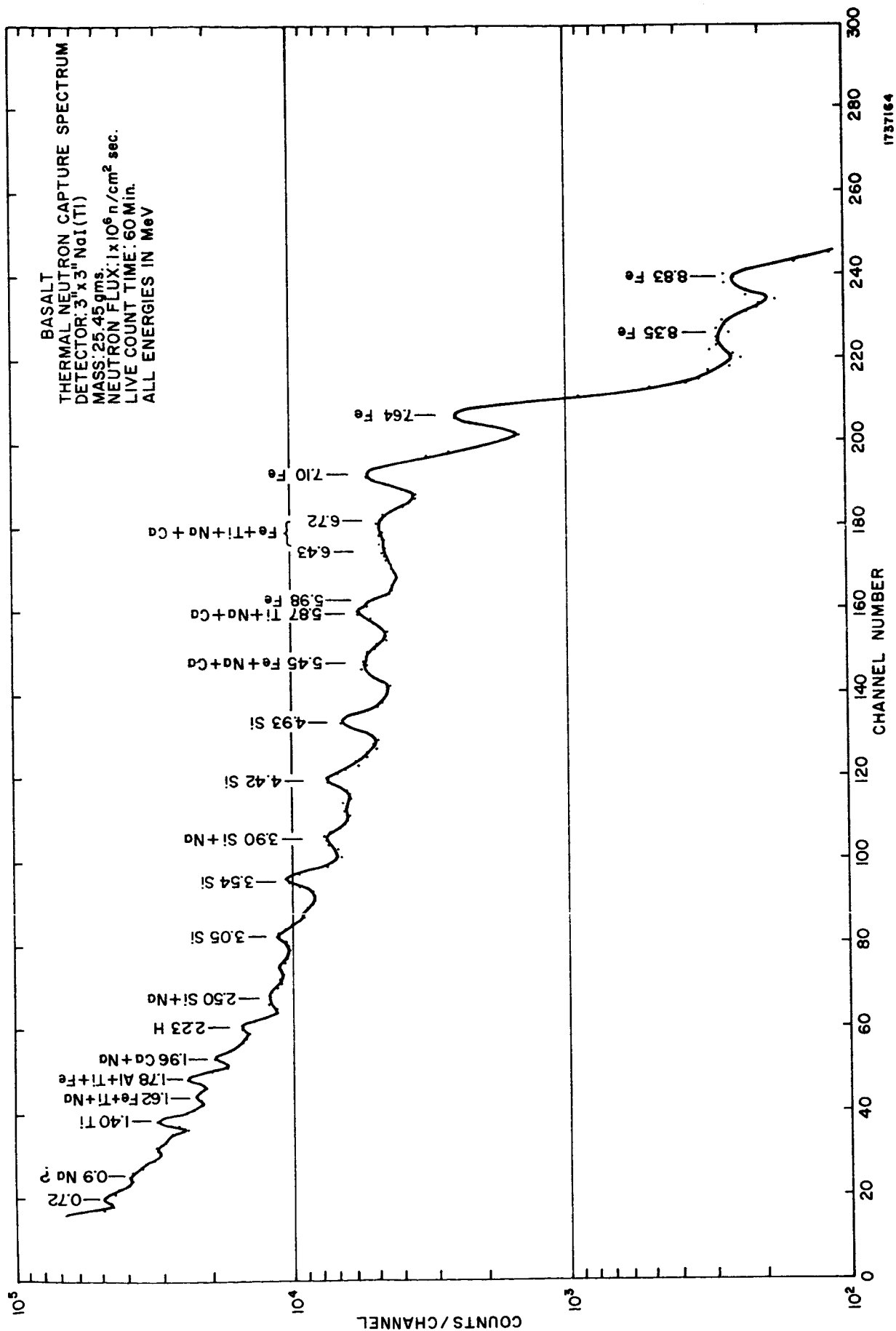


Figure 1  
 CAPTURE GAMMA-RAY SPECTRUM OF BASALT  
 OBTAINED USING NaI(Tl) DETECTOR

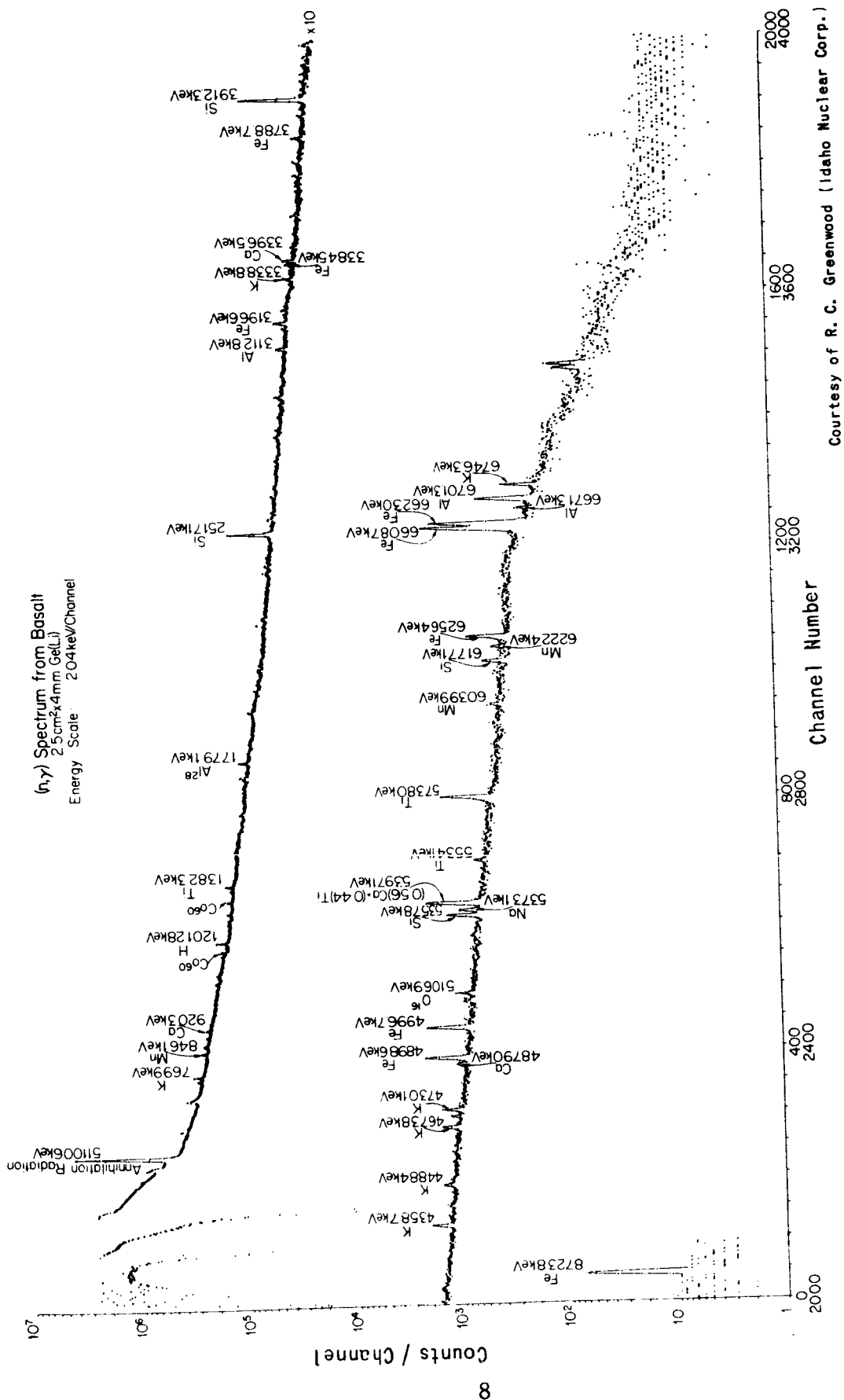


FIGURE 2  
CAPTURE GAMMA-RAY SPECTRUM OF BASALT  
OBTAINED USING Ge(Li) DETECTOR

The complexity of capture gamma-ray spectra results in many interferences between elements when a relatively low resolution detector, such as NaI(Tl), is used. As can be seen readily from a comparison of the two spectra, the improved resolution obtainable from a Ge(Li) detector, as opposed to that from a NaI(Tl) detector, greatly enhances the value of the method by eliminating practically all such interferences. However, since space-hardened Ge(Li) detectors are not as yet available, the present feasibility studies were conducted with a 3 in. x 3 in. NaI(Tl) detector of reasonable resolution (7.2 percent FWHM at 0.662 MeV). Although this restriction decreases the sensitivity of the capture gamma-ray technique, Figure 1 demonstrates that valuable information can be obtained even with a NaI(Tl) detector.

#### Capture Gamma-Ray Analysis Using Fast Neutrons

The capture gamma-ray technique has heretofore required a thermal neutron source and small samples. Since the combined experiment will use a pulsed 14-MeV neutron source and a semi-infinite sample, the feasibility of the capture gamma-ray technique under these conditions has been the subject of the present study. There are a number of areas that have required investigation:

1. The capture gamma-ray technique requires thermal neutrons; therefore, a fraction of the 14-MeV neutrons emitted from the source must be reduced in energy, either by the sample itself or by some other means, to provide a usable thermal flux within the sample. In addition, it is desirable to determine the resultant neutron flux distribution (both thermal and 14 MeV) within a semi-infinite material, since it is this distribution that determines the production of capture gamma rays. The optimum detector position, as well as the degree to which the gamma rays are attenuated and

degraded, depends on the depth and the position in the material from which these gamma rays originate.

Therefore, the effect of several parameters (density, composition, hydrogen content, etc.) on the neutron flux distribution within a semi-infinite material has been examined qualitatively with a one-dimensional transport computer code. The results of these calculations, as well as the experimental flux mapping of a large sand sample, are discussed in Chapter III.

2. While neutron activation and neutron inelastic scattering produce gamma rays of interest to other portions of the combined experiment, these gamma rays constitute background (or noise) for the capture gamma-ray experiment; the interference they produce must therefore be minimized. The pulsed nature of the neutron source can be used to advantage in this regard.

The gamma rays associated with neutron inelastic scatter are prompt, that is, they are present only during the neutron pulse. The capture gamma rays, however, reach a maximum intensity shortly after the neutron pulse (as the neutrons are thermalized), then decay exponentially with a decay constant characteristic of the material (typically 200  $\mu$ sec). Interference from the inelastic gamma rays can therefore be removed by inhibiting the pulse height analyzer (PHA) during the neutron pulse, while these gamma rays are present. The gamma-ray spectrum immediately after each neutron pulse can be sampled (by gating the PHA on) to obtain the composite spectrum of the capture and activation gamma rays.

The activation gamma rays, on the other hand, generally exhibit a half-life which is long compared to the time between pulses. Therefore, a build-up in this type of activity occurs during the neutron

irradiation, and the decay between pulses is negligible. A measure of the activation gamma rays (plus the cosmic ray background) can be made by sampling the gamma spectrum just before each neutron pulse, since most of the capture gamma rays will have decayed away by that time. Thus, by electronically controlling the PHA and by proper choice of neutron pulse repetition rate, the interference from the inelastic gamma rays can be removed and the background produced by neutron activation (and cosmic rays) can be separated from the capture gamma rays.

Figure 3 illustrates schematically the behavior of the three types of gamma rays as a function of time. The time intervals  $S_1$  and  $S_2$  correspond to the times during which the PHA will accept gamma ray counts for the capture experiment. Appendix A shows how to optimize the choice of  $S_1$  and  $S_2$  to achieve the greatest accuracy in the separation of the activation gamma rays from the capture gamma rays.

3. Neutrons interacting with the NaI detector are responsible for a portion of the measured background. These neutrons can result in the production of

- (a) radioactive isotopes, primarily  $I^{128}$  and  $Na^{24}$ ,
- (b) capture gamma rays from iodine and sodium, and
- (c) neutron inelastic scatter gamma rays from iodine and sodium. The effects of the inelastic scatter gamma rays are readily eliminated by gating the PHA off during the pulse, as described above. The experimentation that has been performed to determine the shielding necessary to minimize the production of radioactive isotopes and capture gamma rays within the detector is discussed in Chapter IV.



## CHAPTER III

### DETERMINING THE NEUTRON FLUX DISTRIBUTION WITHIN A SEMI-INFINITE MATERIAL

The combined neutron experiment requires high energy neutrons ( $> 11$  MeV) for the inelastic neutron scatter and fast neutron activation analysis portions of the experiment. The capture gamma ray portion, however, requires the presence of thermal neutrons. Since only one neutron source is to be used in the combined experiment, it is necessary to determine the thermal neutron flux distribution that results within a semi-infinite material when a high energy neutron source is placed on its surface. A discussion of the determination of the thermal neutron flux distribution produced by a high energy neutron source and the factors that influence the flux distribution constitutes the content of this chapter.

#### The High-Energy Neutron Source

The  $T(d,n)He^4$  reaction is a primary source for the production of neutrons with energies in the range 12 to 30 MeV. Because of the large value of the cross section at a deuteron energy of  $\sim 100$  keV and the large  $Q$  value of 17.6 MeV, this reaction is an ideal source for the production of 14-MeV neutrons utilizing compact low voltage accelerators and thick targets. In addition, the 14-MeV neutrons produced in this reaction are essentially isotropic for deuteron energies below 0.5 MeV.<sup>(3,4)</sup>

Furthermore, for deuterons whose energies are in the hundreds of keV, the only level in  $He^5$  which can be populated is at 16.70 MeV. Since gamma decay of this excited state to the ground state of  $He^5$  is highly forbidden, and since no levels exist in  $He^5$  below 16.70 MeV, the  $T(d,n)He^4$  reaction produces neutrons with no gamma-ray contamination. For

these reasons, the  $T(d,n)He^4$  reaction was chosen by NASA as the source of neutrons to be used for the combined neutron experiment.

### Calculated Thermal Neutron Flux Distribution

The use of such a 14-MeV neutron source for a neutron capture gamma-ray experiment requires the consideration of the thermal neutron distribution that results within a semi-infinite material when an isotropic source is placed on its surface and the parameters that affect this distribution.

A neutron transport computer code (DTK) was used to investigate these areas. This steady state one-dimensional code, which was developed at Los Alamos Scientific Laboratory (LASL), is based on the  $S_n$  method.<sup>(5)</sup> The calculations, using 19 neutron energy groups, were made on the IITRI IBM 7094 computer.

The one-dimensional calculations of the flux distribution within a semi-infinite medium assume the geometry of Figure 4. Since this geometry is only a rough approximation to the actual experimental geometry (Figure 5), care must be exercised in interpreting the results. However, these calculations are helpful in determining the effects of composition, density, hydrogen content, and reflector material on the general features of the neutron flux distribution. These effects will be treated separately below.

#### 1. Effects of Composition and Density

The calculations of neutron flux distribution were performed for three hypothetical materials (see Table 2), with no paraffin reflector above the source.

Material I - Hypothetical Lunar  
Surface

Material II - Reflector  
(if used)

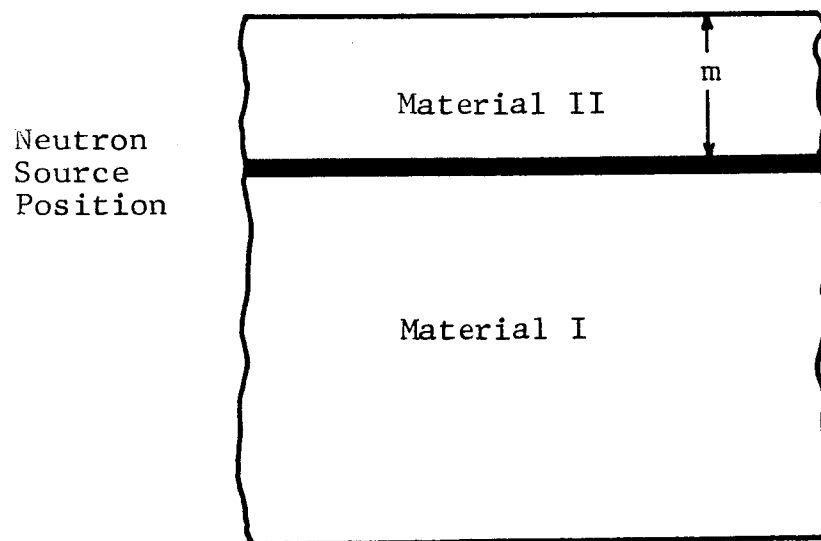
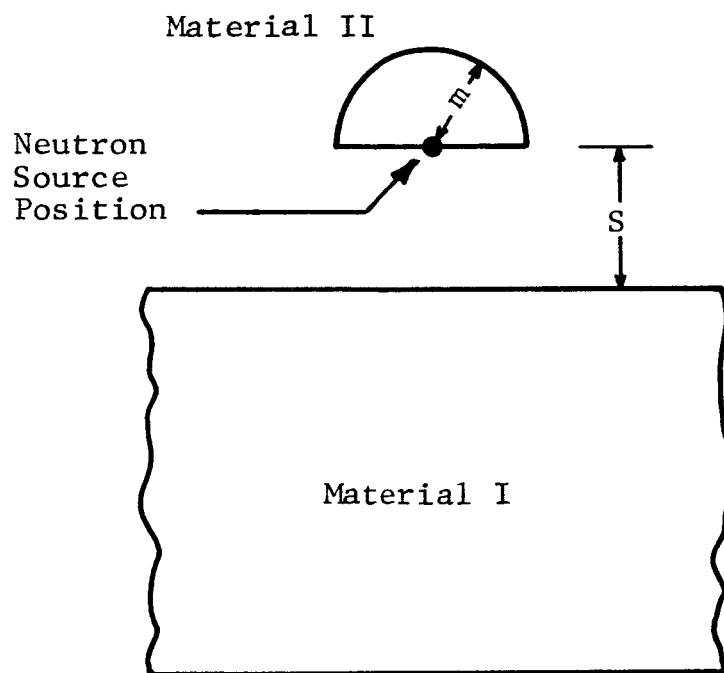


FIGURE 4

ONE DIMENSIONAL GEOMETRY USED FOR COMPUTER CALCULATIONS



Material I - Hypothetical  
Lunar Surface

Material II - Reflector  
(if used)

FIGURE 5

EXPERIMENTAL GEOMETRY

Table 2  
ASSUMED SAMPLE COMPOSITIONS FOR COMPUTER CALCULATIONS

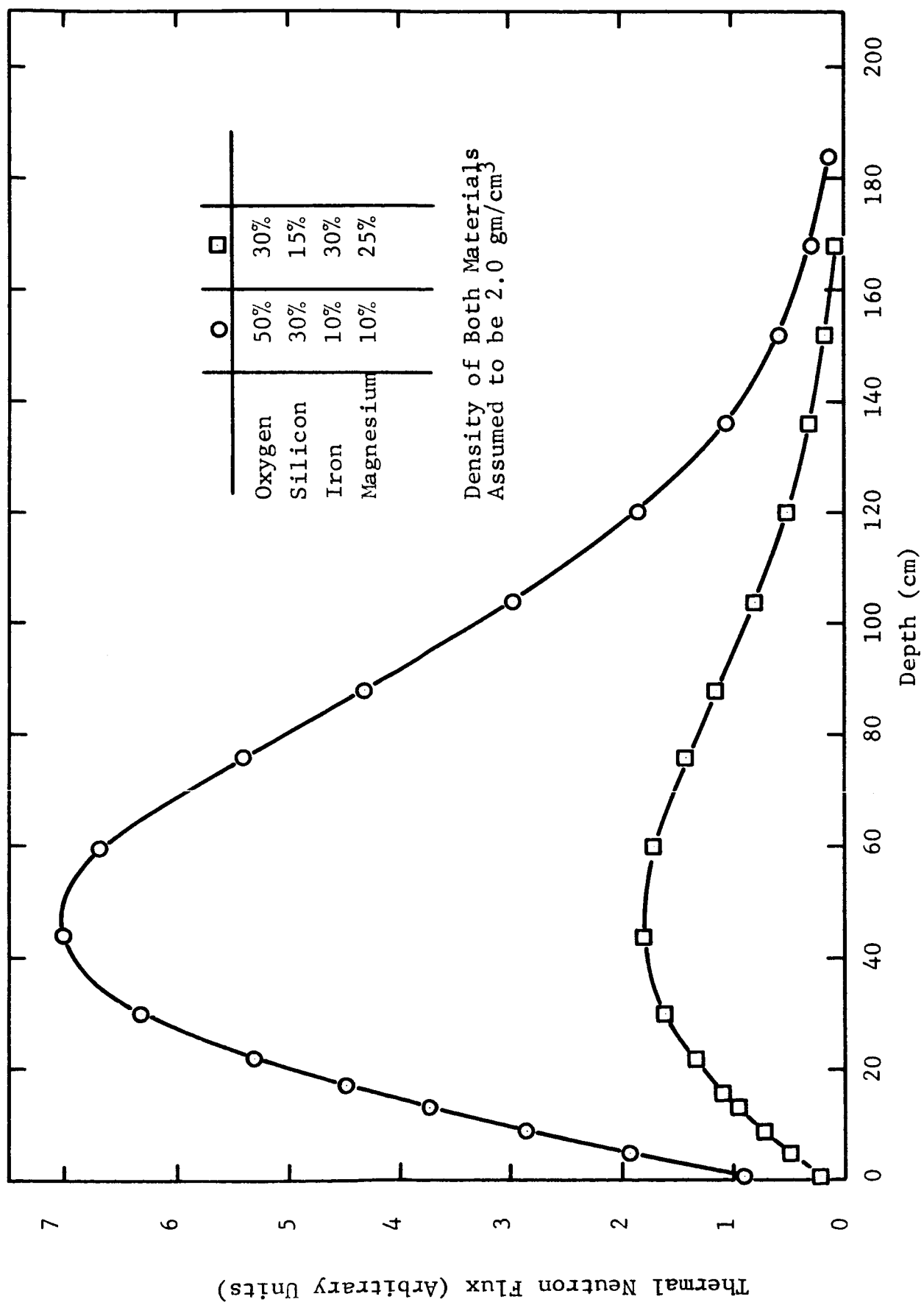
	<u>Wt% O</u>	<u>Wt% Si</u>	<u>Wt% Fe</u>	<u>Wt% Mg</u>	<u><math>\rho</math> (gm/cm<sup>3</sup>)</u>
Material A	50	30	10	10	2.0
Material B	30	15	30	25	2.0
Material C	50	30	10	10	1.0

Figure 6 compares the calculated thermal neutron flux distribution (flux as a function of depth) in materials A and B. The maximum thermal neutron flux occurs at a depth of about 45 cm independent of the bulk composition. The magnitude of the thermal flux is lower in material B than in material A because of the relatively large thermal neutron reaction cross section of iron. Perhaps the most significant result of these calculations is that the thermal neutron flux reaches a maximum at an appreciable distance below the surface (90 gm/cm<sup>2</sup>), which implies that the bulk of the thermal neutron capture gamma rays must penetrate relatively large thicknesses of material if they are to be observed.

The results of the comparison of materials A and C suggest that, as one would expect, the density has no effect on the depth (in gm/cm<sup>2</sup>) at which the thermal neutron flux is maximum.

## 2. Effects of Hydrogen Content

Since hydrogen could be present on the lunar surface in the form of water of hydration, calculations have been made with the DTK code to determine the effect a reasonable hydrogen concentration might have on the thermal neutron flux distribution. As expected,



THE EFFECT OF GROSS COMPOSITION  
ON THE THERMAL NEUTRON FLUX DISTRIBUTION

FIGURE 6

hydrogen facilitates thermalization (see Figure 7). As the hydrogen content increases, the maximum in the thermal neutron flux distribution approaches the surface; however, even with an assumed hydrogen concentration as high as 0.1 percent ( $\sim 1$  percent  $H_2O$ ), the peak in the thermal flux is still about 70 gm/cm<sup>2</sup> below the surface. Thus, it can be concluded that the presence of hydrogen (within reasonable limits) does not greatly perturb the thermal flux distribution.

### 3. Effects of Reflector

With an isotropic neutron source placed above the surface of a semi-infinite material, only half the neutrons strike the material, the other half being lost to the atmosphere. It would be highly desirable if a technique could be found which would make use of these neutrons. A low-Z material placed above the source would reflect some of these neutrons into the surface, thereby increasing the low energy neutron flux without decreasing the fast neutron flux incident on the surface. This increased low-energy neutron flux will increase the sensitivity of the neutron capture gamma-ray technique.

One-dimensional calculations were made using the DTK code assuming the geometry to be that shown in Figure 4. The results are shown in Figure 8. The reflector was assumed to have the composition of light water and to have variable thickness (0, 4 cm, 8 cm, and 13 cm). The 8-cm results are not included in Figure 8, since they are nearly indistinguishable from the 13-cm thickness results. The calculations indicate that the thermal neutron flux is greatly increased near the surface and, in fact, is a maximum at the surface. It is expected that this calculation may have large errors associated with it because of the assumed geometry.

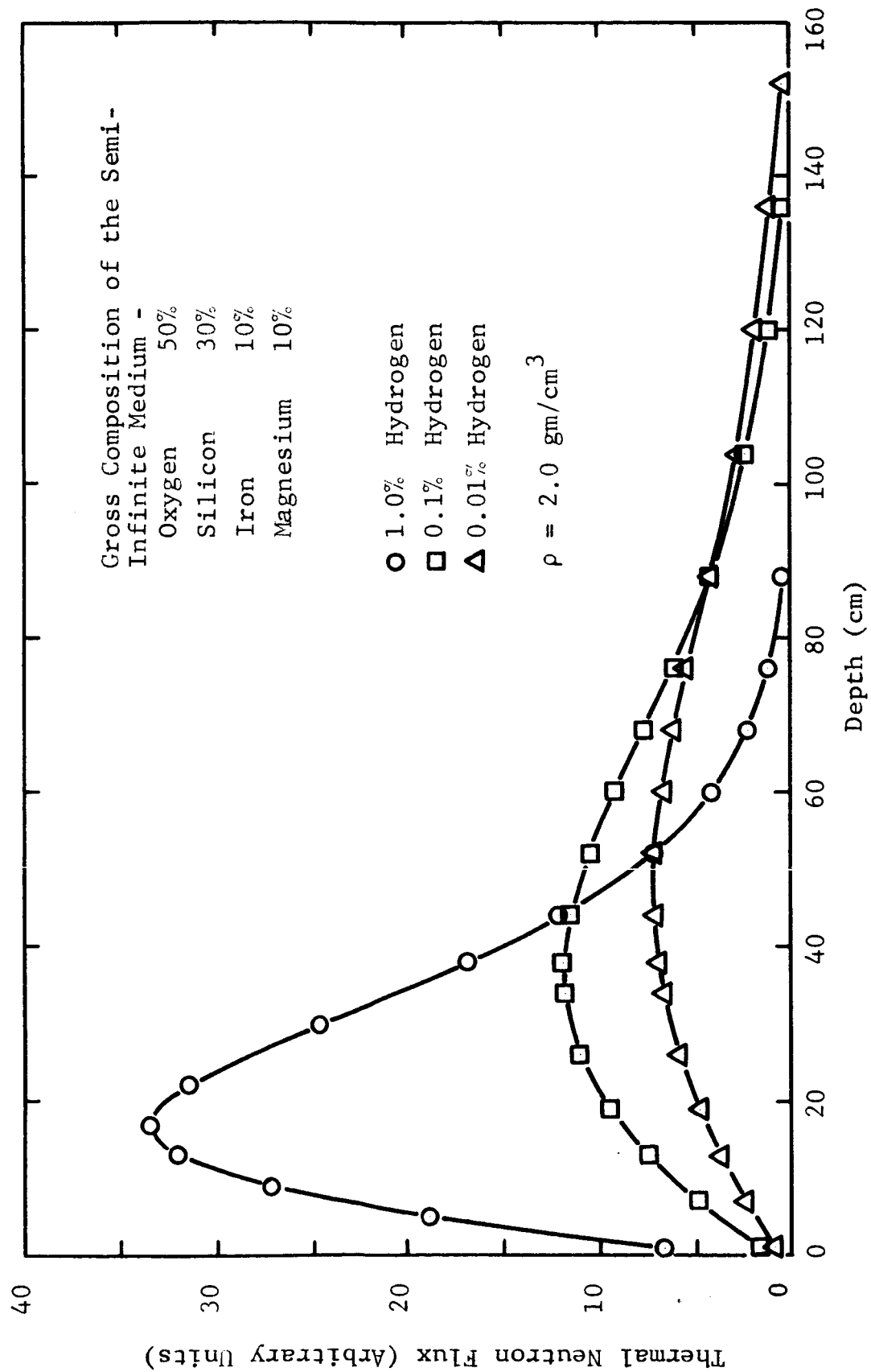


FIGURE 7  
THERMAL NEUTRON FLUX DISTRIBUTION  
AS A FUNCTION OF HYDROGEN CONCENTRATION

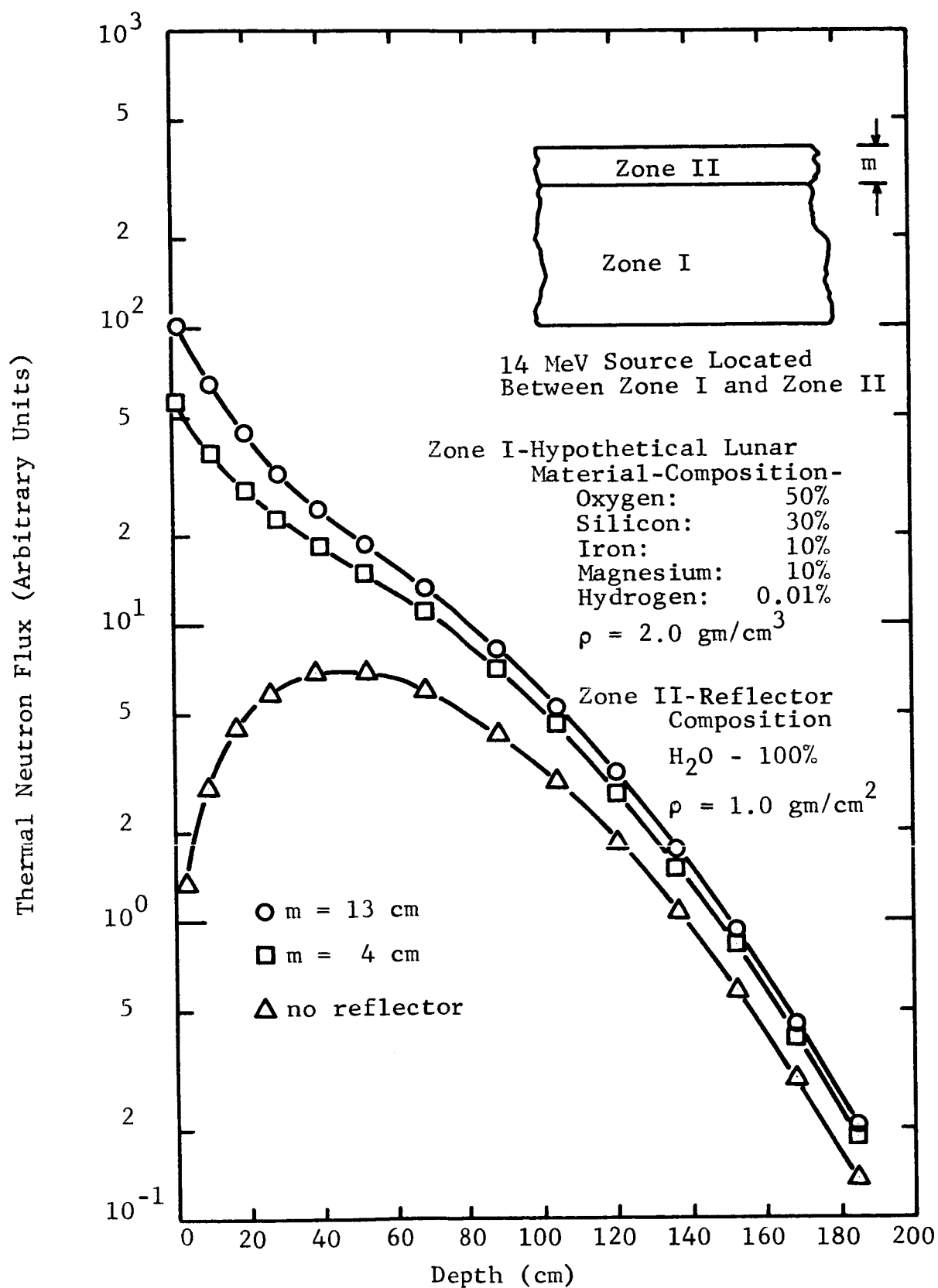


FIGURE 8

THERMAL NEUTRON FLUX DISTRIBUTION  
AS A FUNCTION OF REFLECTOR THICKNESS

This geometry results in a high probability for neutrons to be scattered out of zone I (sample) into zone II (reflector) where the neutrons may again scatter and be returned to zone I. In the actual geometry, the probability for this occurrence is quite small, since the reflector has a small area. However, two conclusions can be drawn: (1) a low-Z material above the neutron source acting as a reflector will increase the thermal flux at the surface, and (2) the thickness of a homogeneous moderator need not be in excess of about  $1.5 \text{ gm/cm}^2$  of hydrogen.

Since the neutron flux distribution within a large sample will exhibit axial symmetry (if the neutron emission is isotropic or axially symmetric), far more realistic results could be obtained if these calculations were performed using two-dimensional transport theory. Several attempts were made to apply the LASL two-dimensional neutron transport code DDK to these calculations. These attempts were unsuccessful because of difficulties in mesh point spacing and the very large demands on core storage.

Since the one-dimensional calculations can provide only a qualitative understanding of the effect of parameters such as composition, density, hydrogen content, and partial reflectors on the thermal neutron flux distribution, one must resort to experimental techniques to get reliable quantitative results.

#### Experimental Determination of the Thermal Neutron Flux Distribution

The thermal neutron flux distribution within a large sample was measured by foil activation. A 60 in. x 60 in. x 30 in. sand sample provided a very convenient approximation to a semi-infinite medium. The specifications supplied by the

manufacturer indicated that the sand was kiln-dried and contained 99.88 percent  $\text{SiO}_2$  with a density of  $1.6 \text{ gm/cm}^3$ . Initial measurements made on the sample showed that there was  $< 0.45$  percent  $\text{H}_2\text{O}$  and that the material bulk density was  $1.74 \text{ gm/cm}^3$ .

Neutron activation foils\* were placed at several locations within the large sample. A combination of bare gold foils and cadmium-covered gold foils was used for the thermal neutron flux measurements. The 14-MeV neutron flux was measured by a copper foil on the sample surface directly below the neutron source. The IITRI Van de Graaff accelerator was used to produce the required 14-MeV neutrons via the D-T reaction. The first irradiation of these foils was made with the neutron source positioned 15 cm above the sample. The copper foil was counted and the 14-MeV neutron flux was determined in accordance with the Texas Convention.<sup>(6)</sup> This same geometry was used to count the gold foils and the cadmium-covered gold foils for determining the thermal neutron flux distribution. A summary of these measurements is presented in Table 3. The thermal flux at the surface was too small to measure; only an upper limit of  $1 \times 10^2 \text{ n/cm}^2 \text{ sec}$  can be assigned. The thermal flux increased with depth and reached a value of  $2.3 \times 10^3 \text{ n/cm}^2 \text{ sec}$  at  $95 \text{ gm/cm}^2$ . The 14-MeV neutron flux incident on the surface directly below the source was  $4.8 \times 10^5 \text{ n/cm}^2 \text{ sec}$ .

A second measurement of the thermal neutron flux was made under the geometry described in Figure 5 with the neutron source again positioned 15 cm above the sample. Paraffin 4 cm thick placed only above the neutron source was used as the reflecting material. The foil activation technique described above was used to measure the resulting neutron flux distribution. The addition of the reflector had a pronounced effect

---

\*The neutron activation foils were obtained from Reactor Experiments, Inc., Belmont, California.

Table 3

THERMAL FLUX DISTRIBUTION IN SAND SAMPLE  
WITHOUT PARAFFIN ABOVE THE SOURCE

---

<u>Position (r,z)</u>	<u>Thermal Flux (n/cm<sup>2</sup> sec)</u>
(0,0)	$< 0.5 \times 10^2$
(0,8 cm)	$0.5 \times 10^2$
(0,16 cm)	$3.5 \times 10^2$
(0,55 cm)	$1.0 \times 10^3$
(14-MeV neutron flux at (0,0) - $2.1 \times 10^5$ n/cm <sup>2</sup> sec)	

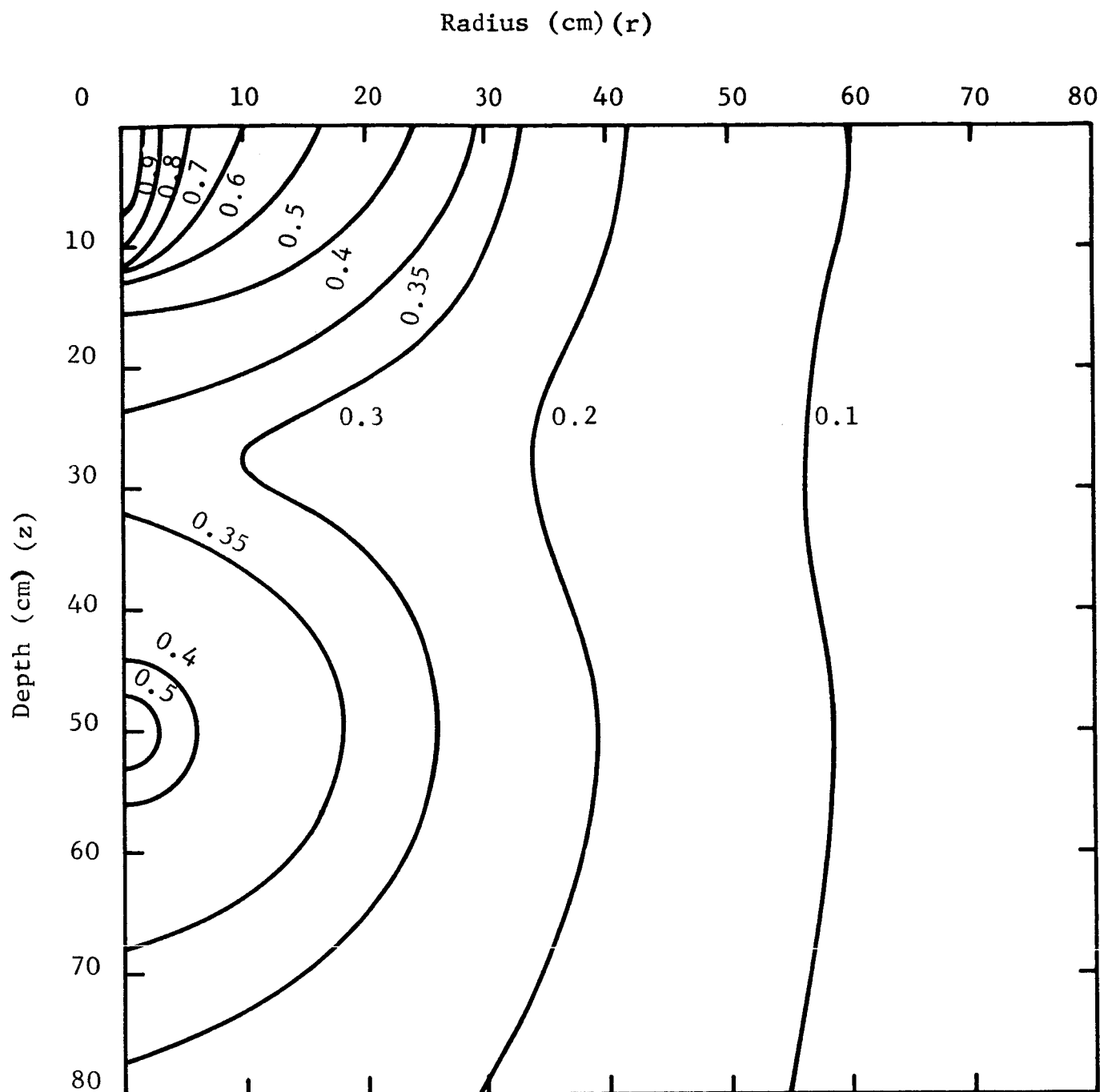
---

on this distribution. The most important change was that the thermal neutron flux at the surface was increased by a factor of about 100. Details of the measured flux distribution within the sample are presented in Figure 9 and Table 4.

To check the isotropy of the neutron source, copper foils were placed at 0 degrees and 90 degrees with respect to the deuteron beam. It was found that the flux at 0 degrees was a factor of 2.6 higher than the flux at 90 degrees. Since the neutron flux emitted at 90 degrees must pass through a target holder composed of copper and aluminum, the difference between the 0 degree and 90 degree flux could be due to scattering in the target holder. The calculation performed to estimate the loss in the 14-MeV flux due to scattering in the target holder indicated that about one-half of the flux is lost. Therefore, while the neutron output of the target is approximately isotropic, the effective 14-MeV flux is peaked in the forward and backward directions by scattering in the target holder material.

### Conclusion

The agreement between the computer predictions and the experimental measurements is quite good. As predicted, the thermal flux, in the absence of any reflector material, increases monotonically with increasing depth down to  $95 \text{ gm/cm}^2$ . With a 4-cm-thick paraffin reflector above the 14-MeV neutron source, the thermal flux at the surface is increased by a factor of 100 and has its maximum value there.



Thermal Flux Values are Relative to Thermal Flux at the Origin

Thermal Flux at Origin:  $3.3 \times 10^3 \text{ n/cm}^2/\text{sec}$   
 14 MeV Flux at Origin:  $2.1 \times 10^5 \text{ n/cm}^2/\text{sec}$

FIGURE 9

CONTOUR PLOT OF THE THERMAL FLUX DISTRIBUTION  
 IN SAND SAMPLE WITH 4 cm OF REFLECTOR  
 ABOVE THE NEUTRON SOURCE  
 AND SOURCE 15 cm ABOVE THE SAMPLE

Table 4  
THERMAL FLUX DISTRIBUTION IN SAND SAMPLE  
WITH PARAFFIN ABOVE THE SOURCE

<u>Position (r,z)</u>	<u>Thermal Flux (n/cm<sup>2</sup> sec)</u>
(0,0)	$3.3 \times 10^3$
(0,8 cm)	$3.0 \times 10^3$
(0,16 cm)	$1.3 \times 10^3$
(0,55 cm)	$1.6 \times 10^3$
(14-MeV neutron flux at (0,0) - $2.1 \times 10^5$ n/cm <sup>2</sup> sec)	

## CHAPTER IV

### EXPERIMENTAL APPARATUS AND PROCEDURE

To establish the practicability of using thermal neutron capture gamma rays as part of NASA's combined neutron experiment, the determination of (1) the feasibility of analysis of a semi-infinite material by means of the capture gamma-ray technique using a pulsed 14-MeV neutron source and (2) the effect on sensitivity of integration with the other neutron techniques are required. Therefore, a parametric study was made to determine the effect of a number of variables on the sensitivity of the technique. A description of the experimental apparatus and procedure used for this parametric study follows, and the results are discussed in Chapter V.

#### Neutron Source

The IITRI Van de Graaff generator was used to produce the 14-MeV neutrons for the capture gamma-ray experiments via the  $T(d,n)He^4$  reaction. The Van de Graaff was operated in a pulsed mode with an accelerating voltage of 0.5 MeV and a beam current of 5  $\mu$ amps. The positive voltage stability is  $\pm 10$  keV and the ion current stability is  $\pm 10$  percent. In the pulsed mode the rise and decay times of the pulses are both less than 3  $\mu$ sec. The pulse rates and durations that were used are 500 pps with 50  $\mu$ sec pulses and 1000 pps with 10  $\mu$ sec pulses. An air-cooled, tritium-titanium target with a 10-mil-thick copper backing was used.

With an accelerating voltage of 0.5 MeV, the theoretical neutron output for the  $T(d,n)He^4$  reaction is approximately  $1.4 \times 10^8$  neutrons/ $\mu$ amp-sec. Experimental results obtained using copper activation foils (cf. Chapter III) indicated that the actual output varied between  $1.3 \times 10^8$  and  $1.7 \times 10^8$  neutrons/ $\mu$ amp-sec. Because of this variation in the neutron

output, a  $\text{BF}_3$  counter was used to monitor the neutron output of the accelerator during the capture gamma-ray experiments. The  $\text{BF}_3$  counter was positioned under the large sample container directly beneath the target, and measured the thermal neutrons diffusing through the sample. Neutron output measurements were performed using copper activation foils to obtain the neutron output per  $\text{BF}_3$  count for each sample. Thus, for a given sample, a  $\text{BF}_3$  count rate could be related directly to neutron output. The calibration of the  $\text{BF}_3$  counter was checked before and after each capture gamma-ray measurement using a Pu-Be neutron source mounted in a fixed geometry, source-counter holder.

#### Gamma-Ray Detection

The detection of the capture gamma rays was accomplished by a 3 in. x 3 in.  $\text{NaI(Tl)}$  crystal optically coupled to a RCA 8054 photomultiplier (PM) tube. Neutrons striking the crystal can interact with the crystal, producing capture gamma rays and gamma rays from the decay of radioactive daughters (e.g.,  $\text{I}^{128}$ ). Both of these effects cause the background count rate to increase. Therefore, it was desirable to shield the crystal from both the 14-MeV and the thermal neutrons. Several shadow shields in the form of truncated cones of carbon and copper were studied to shield the crystal from the 14-MeV neutrons emitted by the source. Also, thermal neutron shields composed of boral ( $\text{Al} + \text{B}_4\text{C}$ ) and  $\text{Li}^6\text{F}$  were investigated. These studies consisted of measuring the relative  $\text{I}^{128}$  activity produced in the crystal while using the various shields. Table 5 lists the results of these investigations.

The most practical shield combination was found to be a 6-in. copper shadow shield and a  $\text{Li}^6\text{F}$  ( $47 \text{ mg/cm}^2 \text{ Li}^6$ ) thermal neutron shield. The 6-in. copper shadow shield was chosen as preferable to the 12-in. carbon shadow shield because the former

Table 5  
RELATIVE EFFICIENCIES OF SHIELDS FOR  
NEUTRON SHIELDING OF THE CRYSTAL

Shield Configuration		Relative Shielding Efficiency
Thermal Shield	Shadow Shield	
None	None	0.5
Boral	None	0.7
Li <sup>6</sup> F	None	0.7
Boral	6-in. carbon	0.9
Boral	12-in. copper	0.9
Boral	6-in. copper	0.9
Boral	12-in. carbon	1.0

would permit the crystal to be located closer to the neutron source. The  $\text{Li}^6\text{F}$  thermal neutron shield is preferable to the boral shield because the latter requires the addition of 1/2 in. of lead between the crystal and the boral to shield against the 0.477-MeV gamma ray emitted following thermal neutron capture in boron.

### Data Collection

The signal from the PM tube was applied to a solid state preamplifier of unity gain mounted on the base of the detector. The schematic for this preamplifier is shown in Figure 10. The output from the preamplifier was applied to a 512 channel pulse height analyzer (Nuclear Data, model 130). Signal amplification was accomplished through the amplifier internal to the analyzer. A 2000-volt high stability power supply (Hammer model N401) was used to supply high voltage to the PM tube.

Initially, the analyzer was gated on (via the coincidence input) for a preset time after each neutron pulse (e.g., 250  $\mu\text{sec}$  to 450  $\mu\text{sec}$  after the beginning of the neutron pulse) with a dual time base Tektronix model 547 oscilloscope. The capture gamma-ray data were accumulated in the first half of the analyzer memory (channels 1 to 255). The timing cycle was initiated by using the pulse from the A gate of the oscilloscope used to monitor the accelerator beam pulses. A second run was then made to obtain a background spectrum. For this run, the analyzer was gated on for a preset time just before each neutron pulse (e.g., 1750  $\mu\text{sec}$  to 1950  $\mu\text{sec}$  after the previous neutron pulse for a 500 pps pulse rate), and background data were accumulated in the second half of the analyzer memory (channels 257 to 511). The final background-corrected capture gamma-ray spectrum was obtained by subtracting the spectrum in the second half of the analyzer memory from the spectrum in the first half, after normalizing

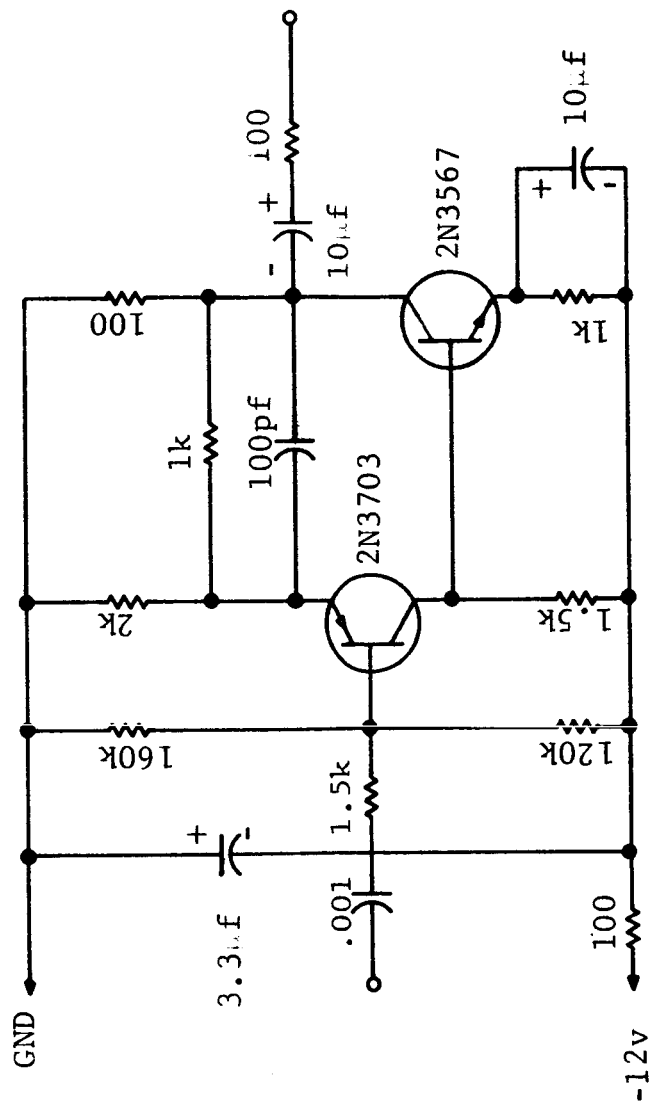


Figure 10 SCHEMATIC DIAGRAM OF THE PREAMPLIFIER

to the total neutron output from the  $\text{BF}_3$  monitor during the capture gamma-ray run.

This method of gating the analyzer with the Tektronix 547 had several drawbacks. Separate runs were necessary for collecting the capture gamma-ray data and the background data, thereby doubling the time necessary for the collection. Since the neutron output of the accelerator can differ during the two runs, the spectra had to be normalized to a given neutron output before background subtraction could be accomplished. Also, only a few sample duration times could be obtained using preset positions on the oscilloscope controls. Most sample duration times and all delay times had to be set using continuously variable controls. This method introduced errors in the accuracy of the determination of these time intervals.

These drawbacks in the method of gating the analyzer led to the design of the analyzer sequence switch (see Figure 11, 11a, 11b). Instead of using the model 547 oscilloscope, the A gate pulse was fed directly into the sequence switch which controlled both the gating of the analyzer (via the coincidence input of the analyzer) and the routing of the signal pulses (via the Set to 0 and Set to 256 inputs of the analyzer). The Set to 0 input is used to route the signal into the first half of the analyzer memory and the Set to 256 input is used to route the signal into the second half of the memory. Delay and sample times were then achieved using known capacitors whose effects on the time intervals were measured using an "events per unit time" meter. Figure 12 is a block diagram showing the operation of the detector and associated electronics.

The analyzer sequence switch affords two modes of operation: "normal" and "alternate". In the "normal" mode both capture gamma-ray and background data are collected after every neutron pulse, while in the "alternate" mode capture gamma-ray data and background data are collected alternately after successive neutron pulses.

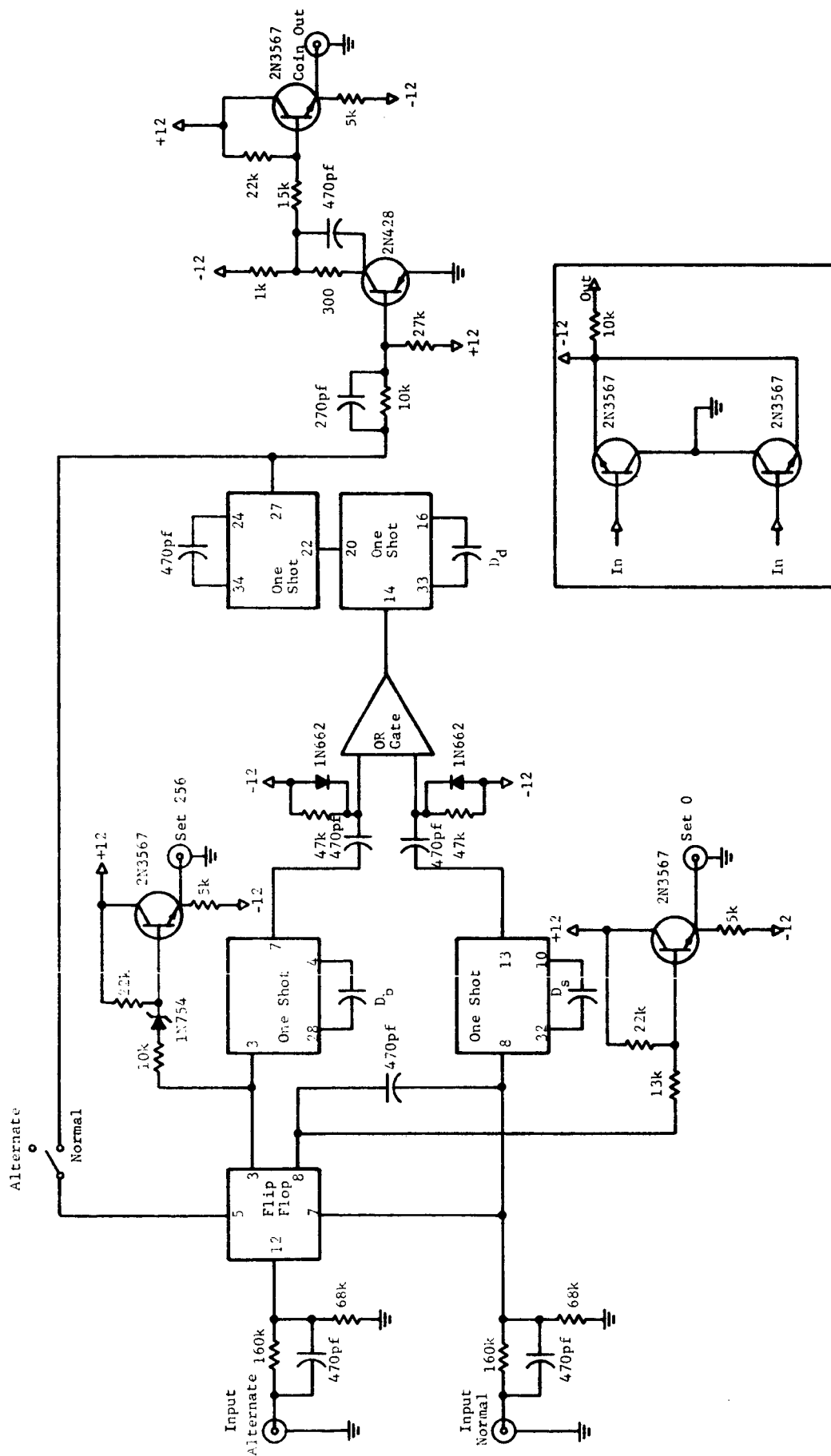


Figure 11  
SCHEMATIC DIAGRAM OF THE ANALYZER SEQUENCE SWITCH

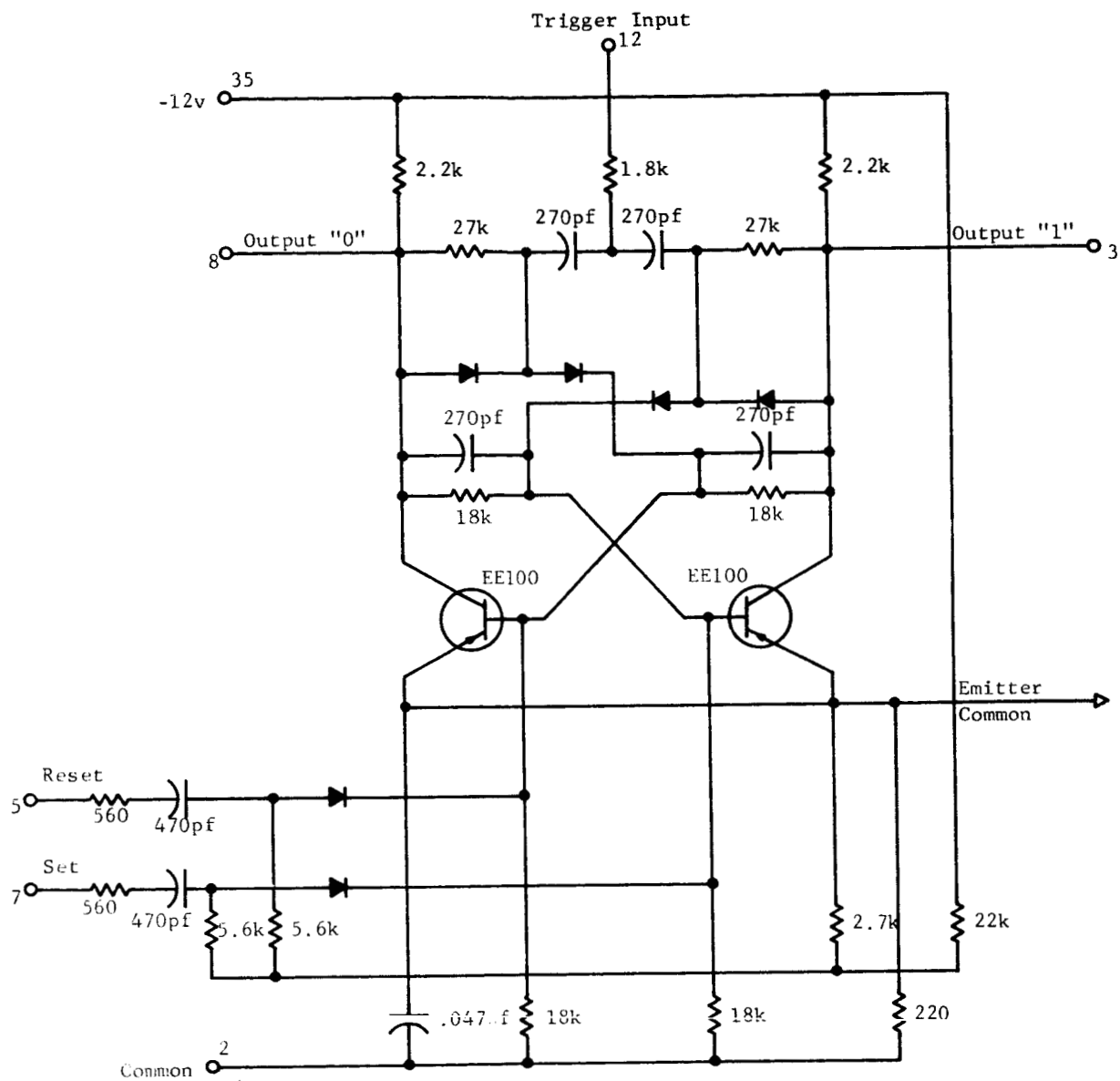


Figure 11a  
SCHEMATIC DIAGRAM OF FLIP FLOP

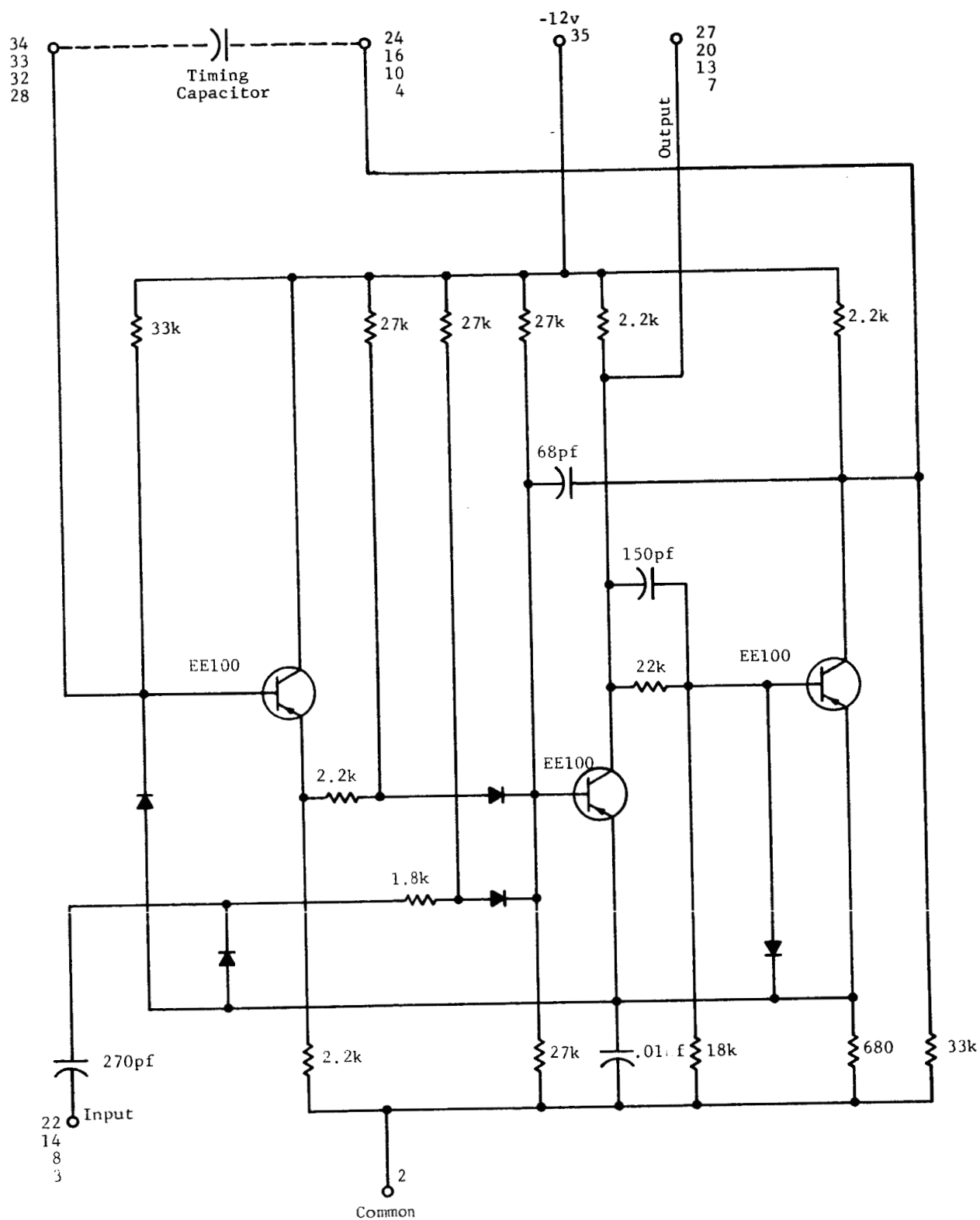


Figure 11b  
SCHEMATIC DIAGRAM OF ONE SHOT

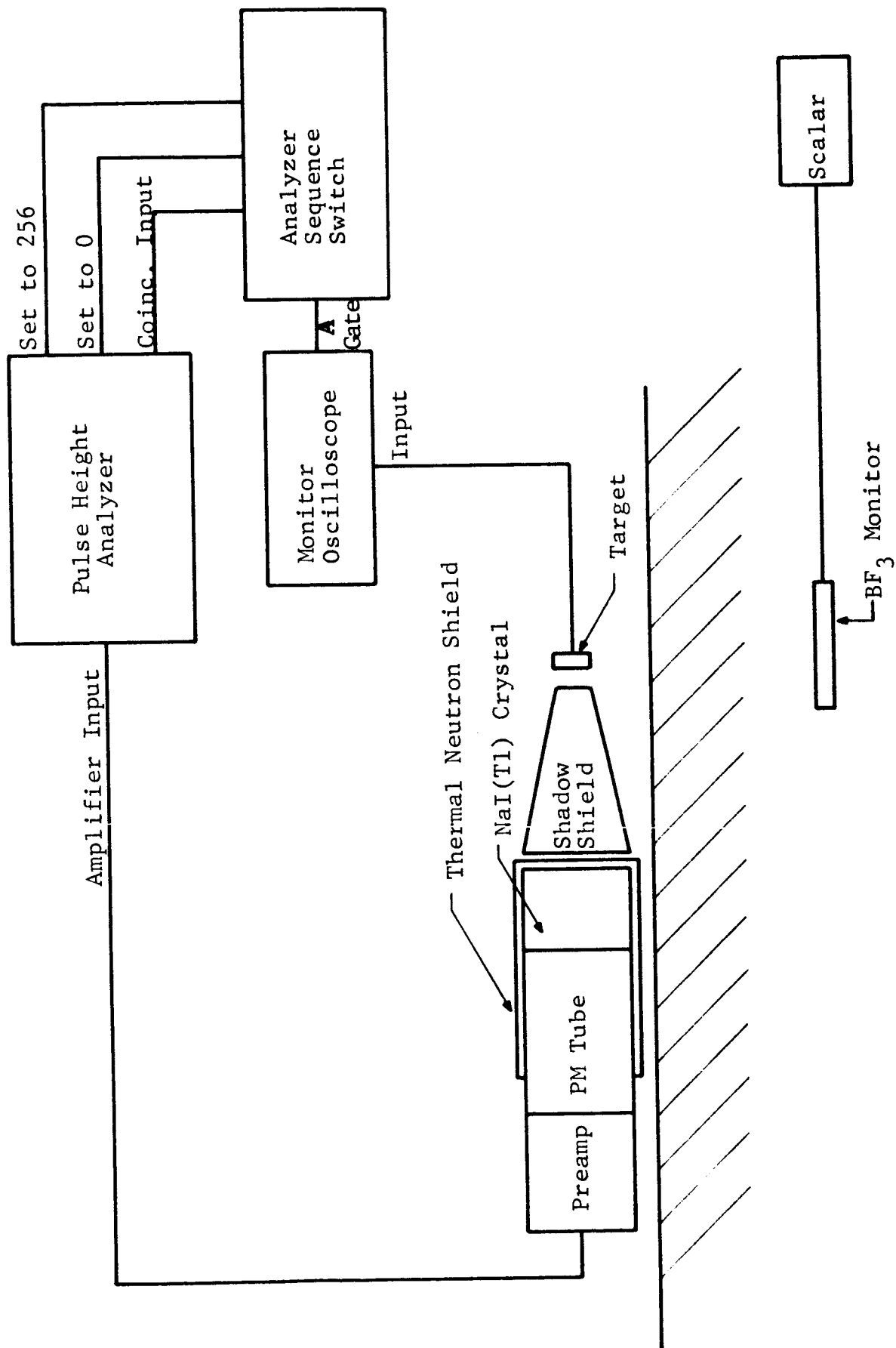


Figure 12  
BLOCK DIAGRAM OF THE DATA COLLECTION SYSTEM

The gating for the "normal" mode results in trace B of Figure 13 being fed into the analyzer coincidence input. As shown by this trace, the analyzer is gated on for a duration  $D_d$  after a delay  $D_s$  after the beginning of each neutron pulse. The capture gamma-ray data collected during this interval are stored in the first half of the analyzer memory. Then (still after the same neutron pulse) the analyzer is gated on again for a duration  $D_d$  after a delay  $D_b$  ( $D_b > D_s$ ) after the beginning of the neutron pulse. The background data collected during this interval are stored in the second half of the analyzer memory. Thus, in this mode capture gamma-ray and background data are collected after every neutron pulse and stored in different halves of the analyzer memory.

The gating for the "alternate" mode results in trace C of Figure 13 being fed into the coincidence input of the analyzer. As shown by this trace, the analyzer is gated on for a duration  $D_d$  after a delay  $D_s$  after the beginning of the first neutron pulse, and the capture gamma-ray data are stored in the first half of the analyzer memory. After the next neutron pulse, the analyzer is gated on for a duration  $D_d$  after a delay  $D_b$  ( $D_b > D_s$ ), and the background data are stored in the second half of the analyzer memory. The next neutron pulse initiates the cycle again. Thus, capture gamma-ray data and background data are collected after the appropriate delays after alternate neutron pulses and stored in different halves of the analyzer memory.

Since the "normal" mode collects data twice as fast as the "alternate" mode, it was used in the parametric study. The "alternate" mode would be used only when the time interval between samples [ $D_b - (D_s + D_d)$ ] is shorter than the time necessary for the analyzer to accept and store a pulse ( $\sim 150 \mu\text{sec}$ ).



### Experimental Sample

The 60 in. x 60 in. x 30 in. sand sample described in Chapter III was used for the capture gamma-ray measurements. Thermal neutron capture gamma-ray spectra from a sample of the sand (Figure 14) and from a sample of pure silicon (Figure 15) were obtained using thermal neutrons from the IITRI Research Reactor (for details of the procedure, see Reference 7). Since only silicon capture gamma-ray lines are observed in Figure 14, it can be concluded that the sand contains no significant amounts of contaminants that produce interfering capture gamma-ray lines.

The first series of capture gamma-ray spectra from the large sand sample taken using the pulsed 14-MeV source of neutrons resulted in the silicon capture gamma rays being nearly obscured by the  $O^{16}(n,p)N^{16}$  fast activation gamma rays. Under these conditions, the silicon capture gamma rays are difficult to use for the study of the effects of various parameters on the detectability of the capture gamma rays. Therefore, iron (in the form of 1/8-in.-thick plates) was added to the sand sample to facilitate the parametric study. The iron capture gamma-ray spectrum (see Figure 16) contains a strong 7.64-MeV gamma ray which, being higher in energy than the  $O^{16}(n,p)N^{16}$  gamma rays, is not obscured by the oxygen activation. The resulting active volume of sample matrix (iron-sand-1) contained 20 percent iron, 43 percent oxygen and 37 percent silicon.

To facilitate the detector-source geometry phase of the parametric study, a second iron-sand matrix (iron-sand-2) was used. In iron-sand-2, a uniform layer of iron was located 5 cm below the surface of the sand. A third iron-sand matrix (iron-sand-3) was also used. This sample resembles iron-sand-1 in iron content but differs slightly in the placement of the iron plates with respect to the source and the sides of the sample container.

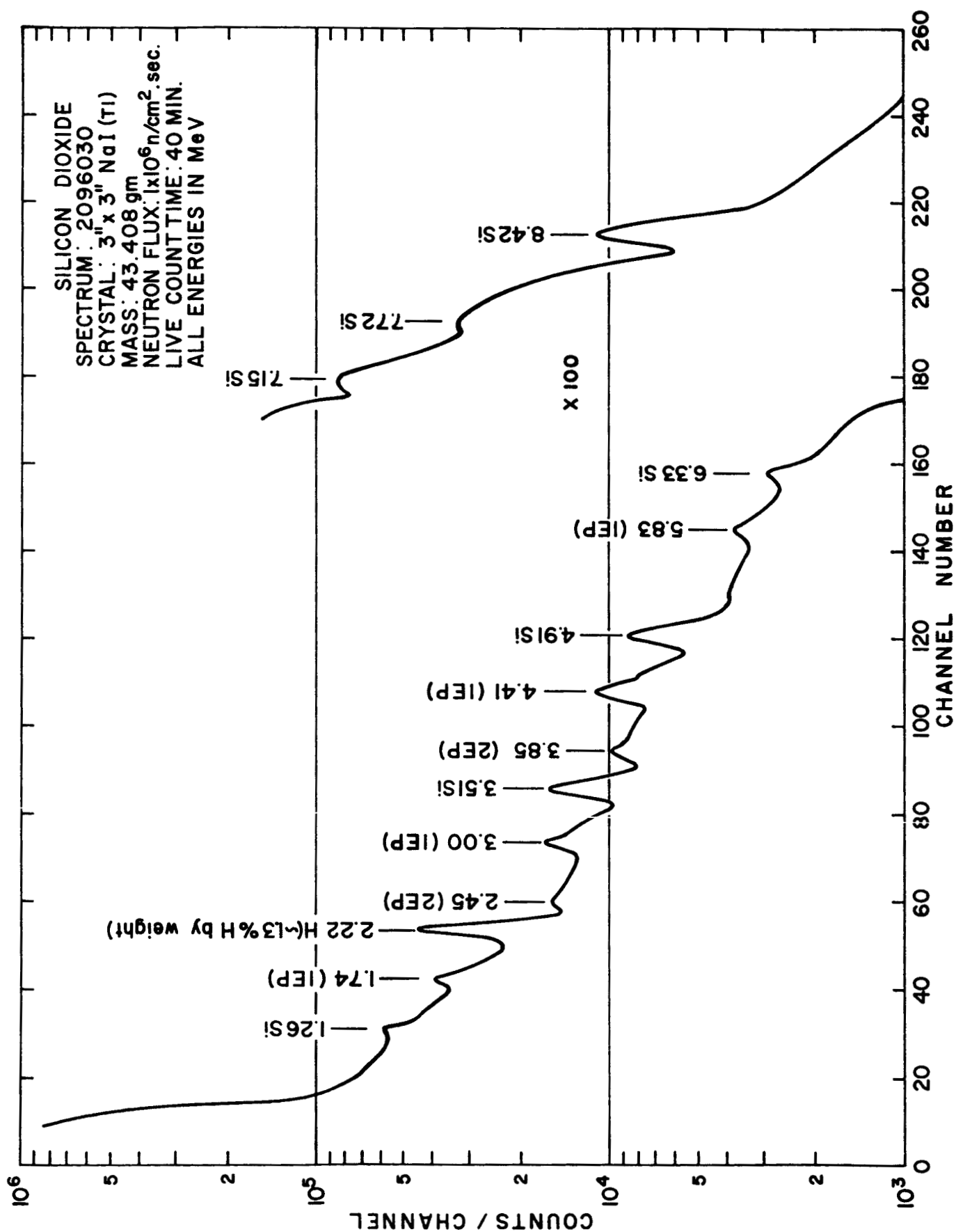


Figure 14  
 CAPTURE GAMMA-RAY SPECTRUM OF SAND

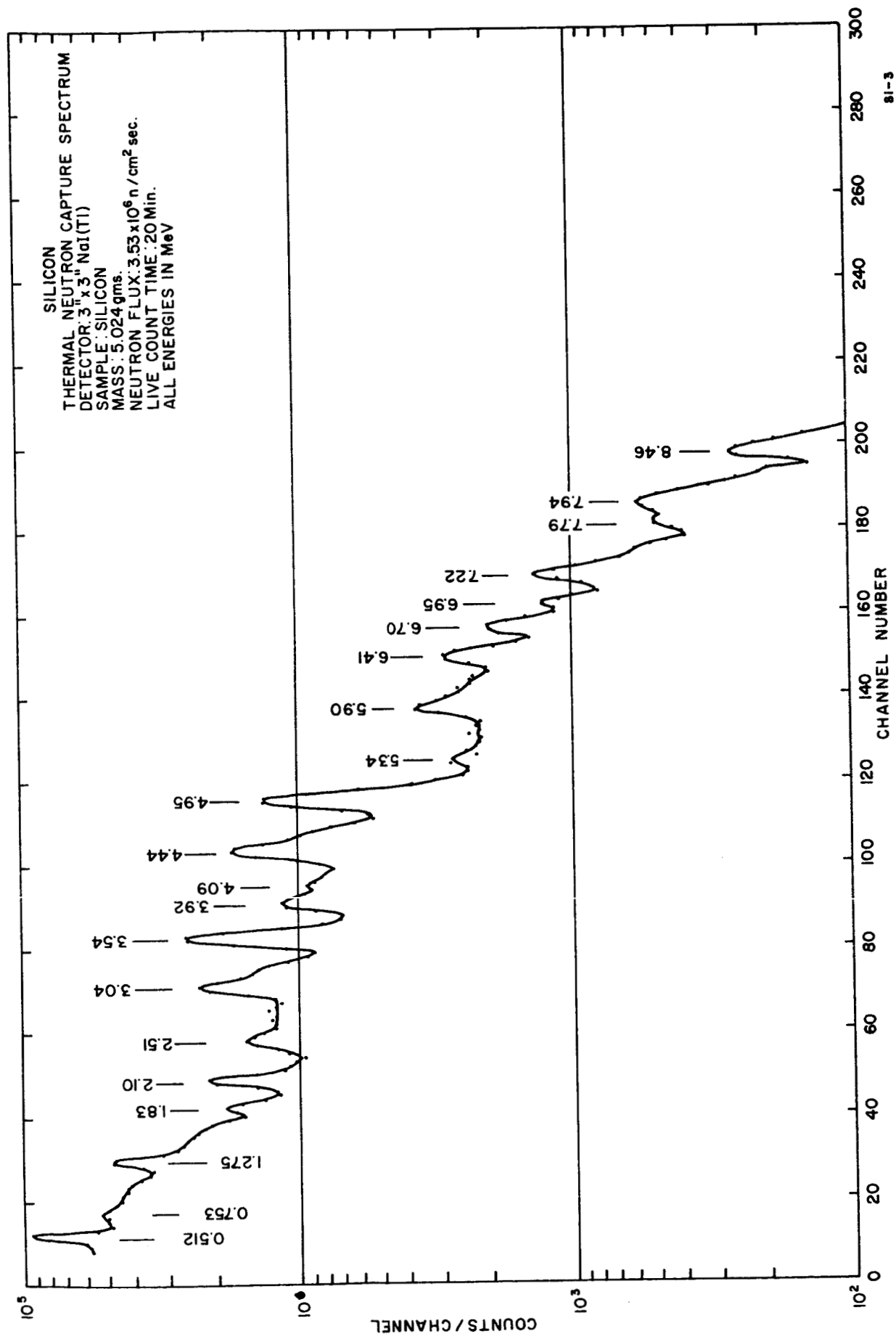


Figure 15  
CAPTURE GAMMA-RAY SPECTRUM OF SILICON

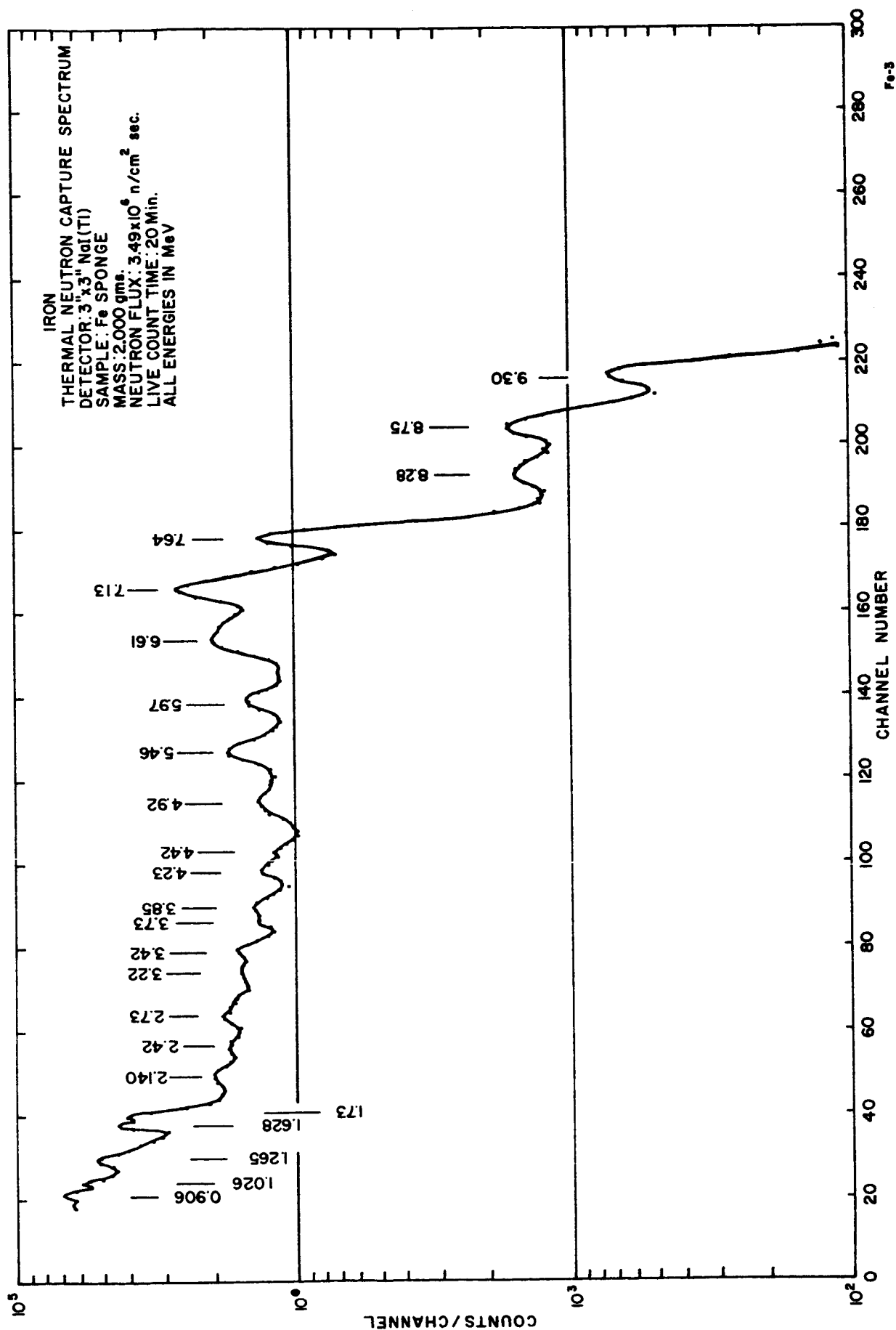


Figure 16  
CAPTURE GAMMA-RAY SPECTRUM OF IRON

## CHAPTER V

### PARAMETRIC STUDY RESULTS

A number of parameters affect the quality of the capture gamma-ray spectra obtained using 14-MeV neutrons and a semi-infinite sample. Some of these are the length of the sampling period, the neutron reflector thickness, the detector-source geometry, and the neutron pulse rate. The optimization of each of these parameters will be discussed individually.

#### Length of Sampling Period

Since the intensity of the capture gamma rays decreases as a function of time after the neutron pulse while the intensity of the background is essentially constant (the 7.4-sec half-life of  $N^{16}$  is long compared to the time between neutron pulses), the length of the sampling period can be chosen to minimize the fractional statistical error in the observed signal after background subtraction. The determination of this optimum sample duration is discussed in Appendix A.

To determine the optimum length of the sampling period, the thermal neutron lifetime in the sample must be known. This was determined experimentally by observing the number of counts in the 7.64-MeV  $Fe(n, \gamma)$  peak as a function of time after the neutron pulse. With a sample duration of 50  $\mu\text{sec}$  and delays varying from 250  $\mu\text{sec}$  to 1900  $\mu\text{sec}$ , the thermal neutron lifetime was found to be 282  $\mu\text{sec}$  in iron-sand-1 sample matrix and 155  $\mu\text{sec}$  in iron-sand-3 sample matrix. The difference in the thermal neutron lifetimes in the two samples was caused by the different placements of the iron plates in the sand.

The value of the signal-to-noise ratio,  $N_0/B$ , must also be known to determine the optimum length of the sampling period.  $N_0$  is the signal count rate at the beginning of the sampling period, and  $B$  is the background count rate (assumed to be

constant). The signal-to-noise ratio was measured to be approximately two for the 7.64-MeV  $\text{Fe}(n,\gamma)$  line at a pulse rate of 500 pps. This measurement was performed by obtaining (1)  $N_0$ , the number of counts in the 7.64-MeV  $\text{Fe}(n,\gamma)$  peak recorded in an interval 200  $\mu\text{sec}$  long, delayed 250  $\mu\text{sec}$  after the neutron pulse, and (2)  $B$ , the background recorded in an interval 200  $\mu\text{sec}$  long, delayed 1700  $\mu\text{sec}$  after the neutron pulse. If the neutron output per pulse remains the same, it is assumed that the background at a 1000 pps pulse rate will be twice that observed with a 500 pps rate, while the capture gamma rays per pulse remain constant (see Appendix A). Therefore, a signal-to-noise ratio of unity is assumed for the 7.64-MeV  $(n,\gamma)$  line with a pulse rate of 1000 pps.

With the method of Appendix A and the above values for  $\tau$  and  $N_0/B$ , it was found that, although an optimum length of the sampling period exists, the fractional error in the signal is quite insensitive to the length of the period. This was found to be true for both values of the thermal neutron lifetime (282  $\mu\text{sec}$  and 155  $\mu\text{sec}$ ) and for both pulse rates (500 pps and 1000 pps).

To facilitate a direct comparison between the two pulse rates for subsequent parametric measurements, it was decided to employ a common sample duration. It is clear that this procedure is justified when one considers that the previous results showed that the sample duration is not critical. The only constraint on the sample duration is that it must be shorter than the maximum length which can be used at the 1000 pps pulse rate. If a background sample is also taken, the necessary 250- $\mu\text{sec}$  delay after the neutron pulse and the analyzer dead time means that the maximum length of the sampling period is 250  $\mu\text{sec}$ . For convenience, the 200- $\mu\text{sec}$  sample duration, which was a precalibrated setting on the oscilloscope, was used when the analyzer was gated by the Tektronix 547 oscilloscope. When the analyzer sequence switch was used for the gating, a sample duration of 230  $\mu\text{sec}$  was used because of the availability of a stable capacitor giving this duration.

### Neutron Reflector Thickness

To determine the optimum thickness of the neutron reflector and the effects of placing a low-Z material between the neutron source and the sample, capture gamma-ray spectra were obtained using several thicknesses of paraffin located both above and below the neutron source. For each case, the relative intensity of the iron capture gamma rays and the relative spectral quality of the spectrum were calculated. The relative intensity of the iron capture gamma rays was determined by integrating the number of counts under the 7.64-MeV  $\text{Fe}(n,\gamma)$  peak per unit 14-MeV neutron output. The relative spectral quality was obtained by taking the ratio of the number of counts under the 7.64-MeV  $\text{Fe}(n,\gamma)$  peak to the number of counts under the 6.13-MeV  $\text{O}(n,p)$  peak. The relative spectral quality, therefore, is a measure of the dominance of the capture gamma rays over the oxygen activation gamma rays. A low value for the spectral quality indicates that the oxygen activation gamma rays dominate the spectrum.

The results of the reflector determination are contained in Table 6. They show that 4 cm of paraffin located above the source increases the  $\text{Fe}(n,\gamma)$  intensity by more than a factor of two and the spectral quality by about 50 percent over the case with no paraffin above the source. If 8 cm of paraffin is located above the source, the  $\text{Fe}(n,\gamma)$  intensity is increased by about a factor of four and the spectral quality by about a factor of two over the case with no paraffin. The spectra obtained using 0, 2, 4, and 8 cm of paraffin above the source are shown in Figures 17 to 20.

The results of the measurements made with paraffin between the source and sample (Table 7) indicate that the  $\text{Fe}(n,\gamma)$  intensity and spectral quality show only a slight increase when paraffin is placed between the neutron source and the sample. Since a moderator between the neutron source and the sample is only slightly beneficial to the capture

Table 6

THE EFFECT OF A REFLECTOR ABOVE THE  
NEUTRON SOURCE ON SPECTRAL RESPONSE

Thickness of Paraffin (cm)	Relative Spectral Quality	Relative Intensity Fe(n, $\gamma$ )
0	0.30	30
2	0.40	50
4	0.45	70
6	0.60	90
8	0.60	120

(No moderator between target and sample.)

(Horizontal geometry: source-to-crystal distance is 52 cm  
and crystal-to-sample distance is 5 cm.)

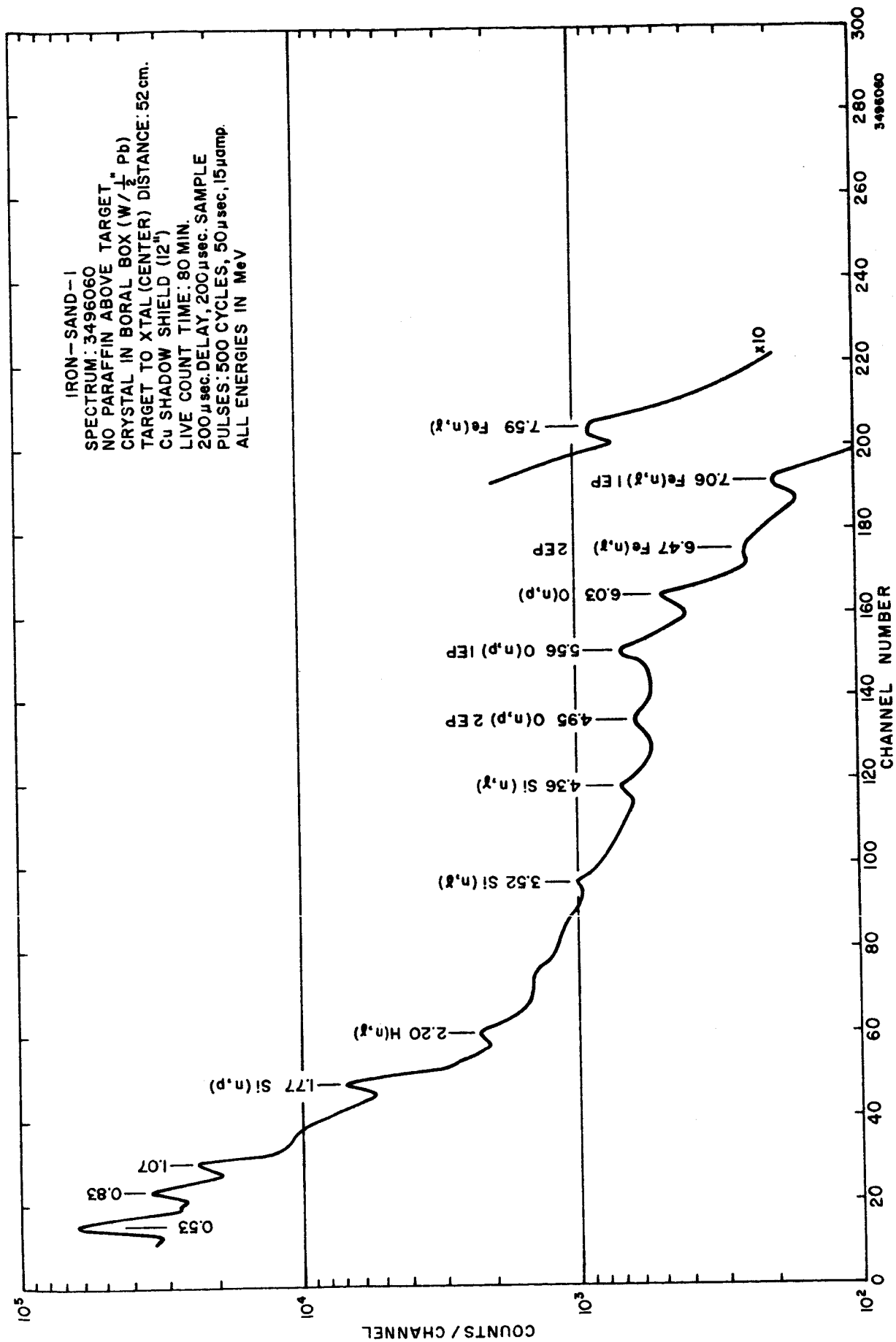


Figure 17  
CAPTURE GAMMA-RAY SPECTRUM OF IRON-SAND SAMPLE  
OBTAINED USING NO PARAFFIN ABOVE TARGET

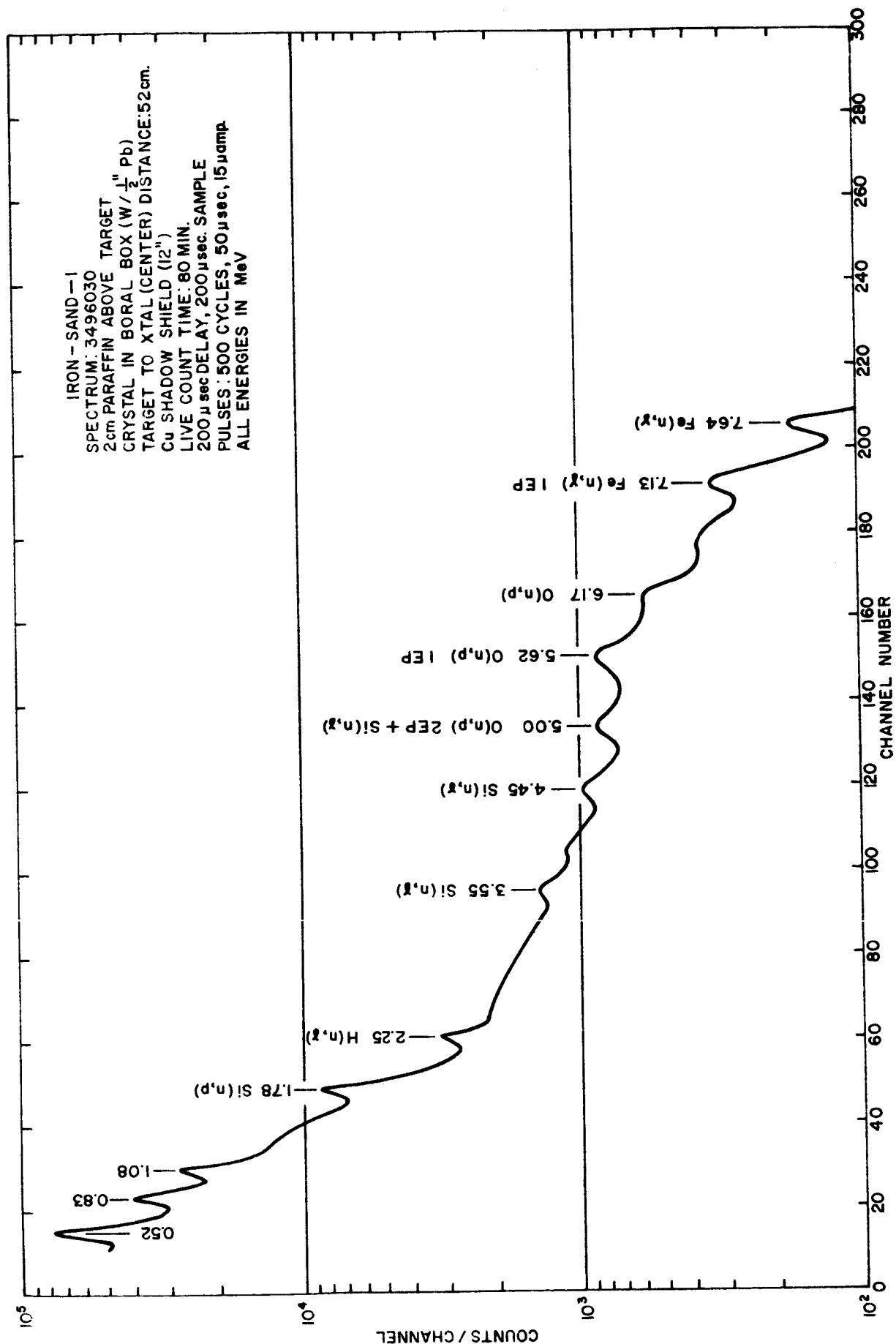


Figure 18  
CAPTURE GAMMA-RAY SPECTRUM OF IRON-SAND SAMPLE  
OBTAINED USING 2cm PARAFFIN ABOVE TARGET

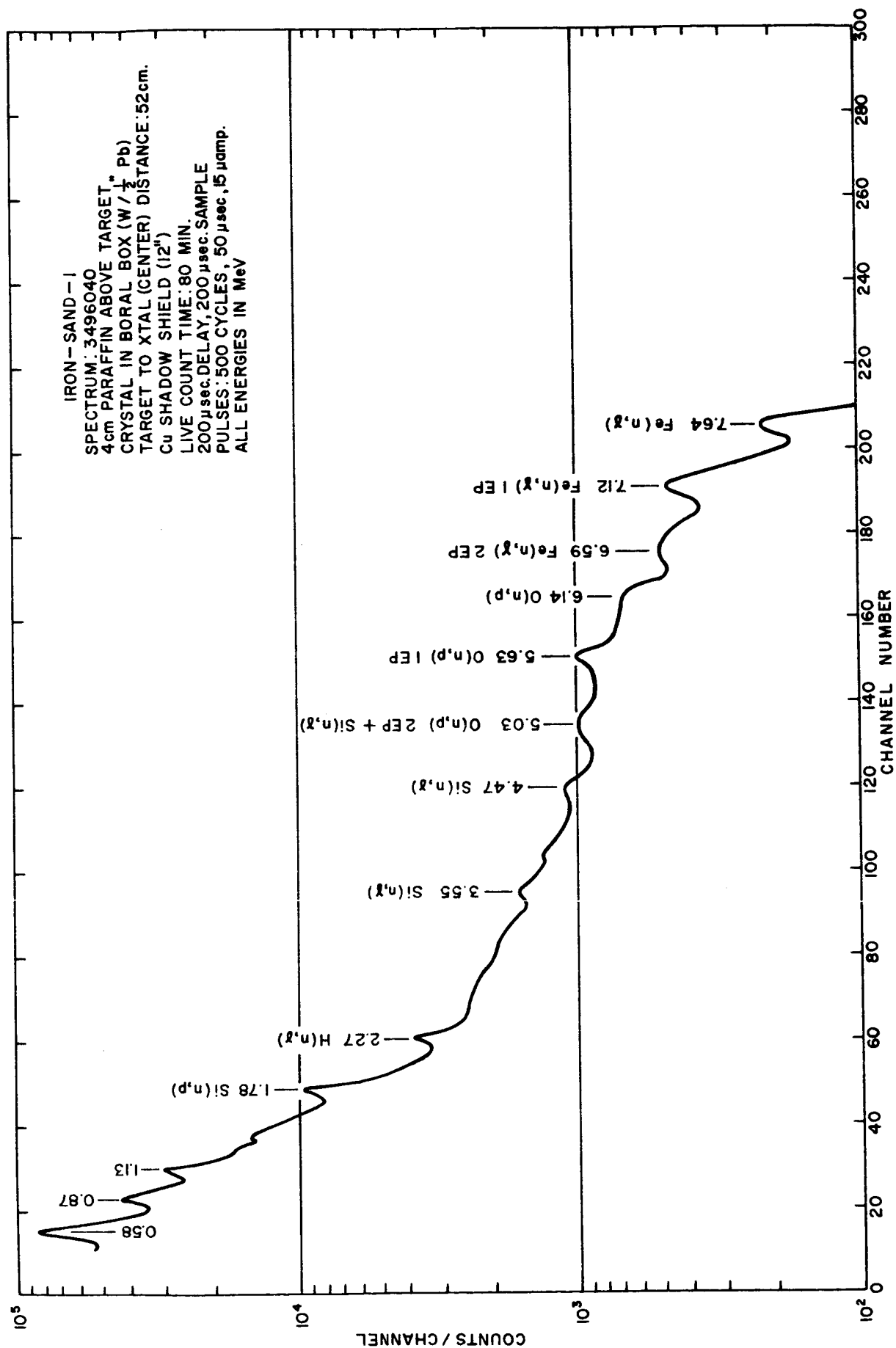


Figure 19  
 CAPTURE GAMMA-RAY SPECTRUM OF IRON-SAND SAMPLE  
 OBTAINED USING 4cm PARAFFIN ABOVE TARGET

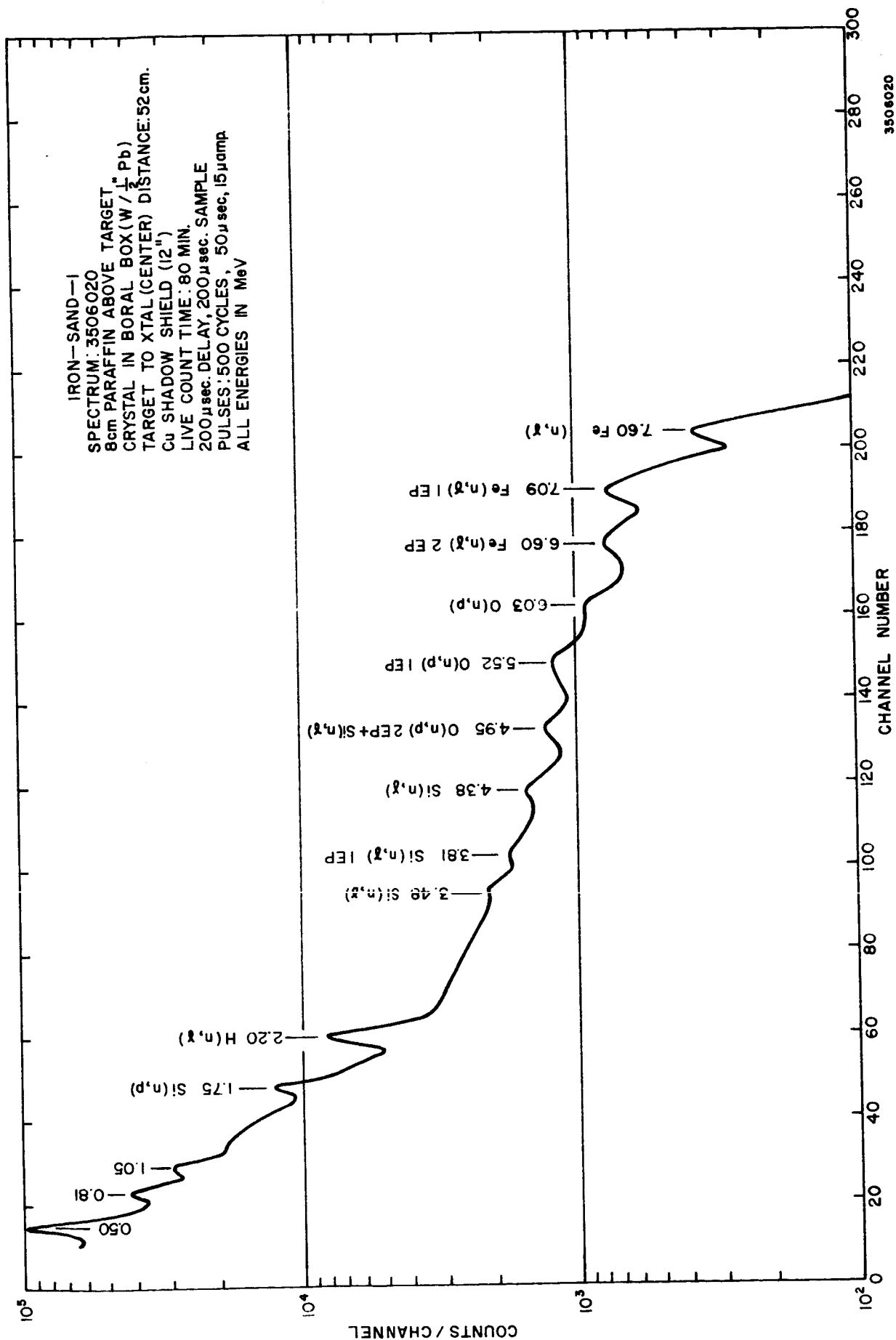


Figure 20  
CAPTURE GAMMA-RAY SPECTRUM OF IRON-SAND SAMPLE  
OBTAINED USING 8cm PARAFFIN ABOVE TARGET

Table 7

THE EFFECT OF A MODERATOR BETWEEN THE TARGET  
AND SAMPLE ON SPECTRAL RESPONSE

Amount of paraffin below target (cm)	Amount of paraffin above target (cm)	Relative Spectral Quality	Relative Intensity $\text{Fe}(n, \gamma)$
0	0	0.25	60
2	0	0.25	60
0	4	0.35	100
2	4	0.40	100
4	4	0.45	130

(Horizontal geometry: source-to-crystal distance is 37 cm and crystal-to-sample distance is 10 cm.)

gamma-ray experiment and is quite detrimental to the inelastic scattering experiment, it will not be used. However, a neutron reflector located above the source greatly increases the sensitivity of the capture gamma-ray technique and has been incorporated into the experiment.

#### Detector-Source Geometry

Two types of detector-source geometries have been considered, horizontal and vertical. In the horizontal configuration, both the source and detector lie in a horizontal plane located a given distance above the surface of the sample. In the vertical configuration, the source and detector lie in a vertical plane with the detector located above the source. Both configurations are shown in Figure 21.

For experimental comparison between the two types of geometries, the iron-sand-2 sample matrix was used. The measurements were made with a 8-cm-thick paraffin reflector located above the neutron source and the source located 5 cm above the surface of the sample. For each geometry, two different source-to-crystal distances were used, 37 cm and 52 cm with the horizontal geometry, and 32 cm and 47 cm with the vertical geometry. Plots of the spectra (both capture gamma ray and background) obtained are shown in Figures 22 to 25.

For each geometry and source-to-crystal distance, the relative  $\text{Fe}(n,\gamma)$  intensity and the spectral quality index were measured. The relative  $\text{Fe}(n,\gamma)$  intensity was obtained by integrating the number of counts under the 7.64-MeV  $\text{Fe}(n,\gamma)$  peak after background subtraction and then normalizing to a given 14-MeV output. The spectral quality index denotes the ratio of the  $\text{Fe}(n,\gamma)$  to  $\text{O}(n,p)$  gamma-ray intensities. It is obtained by taking the ratio of the counts under the 7.64-MeV  $\text{Fe}(n,\gamma)$  peak after background subtraction to the counts under the 6.13-MeV  $\text{O}(n,p)$  peak in the background (long delayed spectrum). The results listed in Table 8 indicate that the

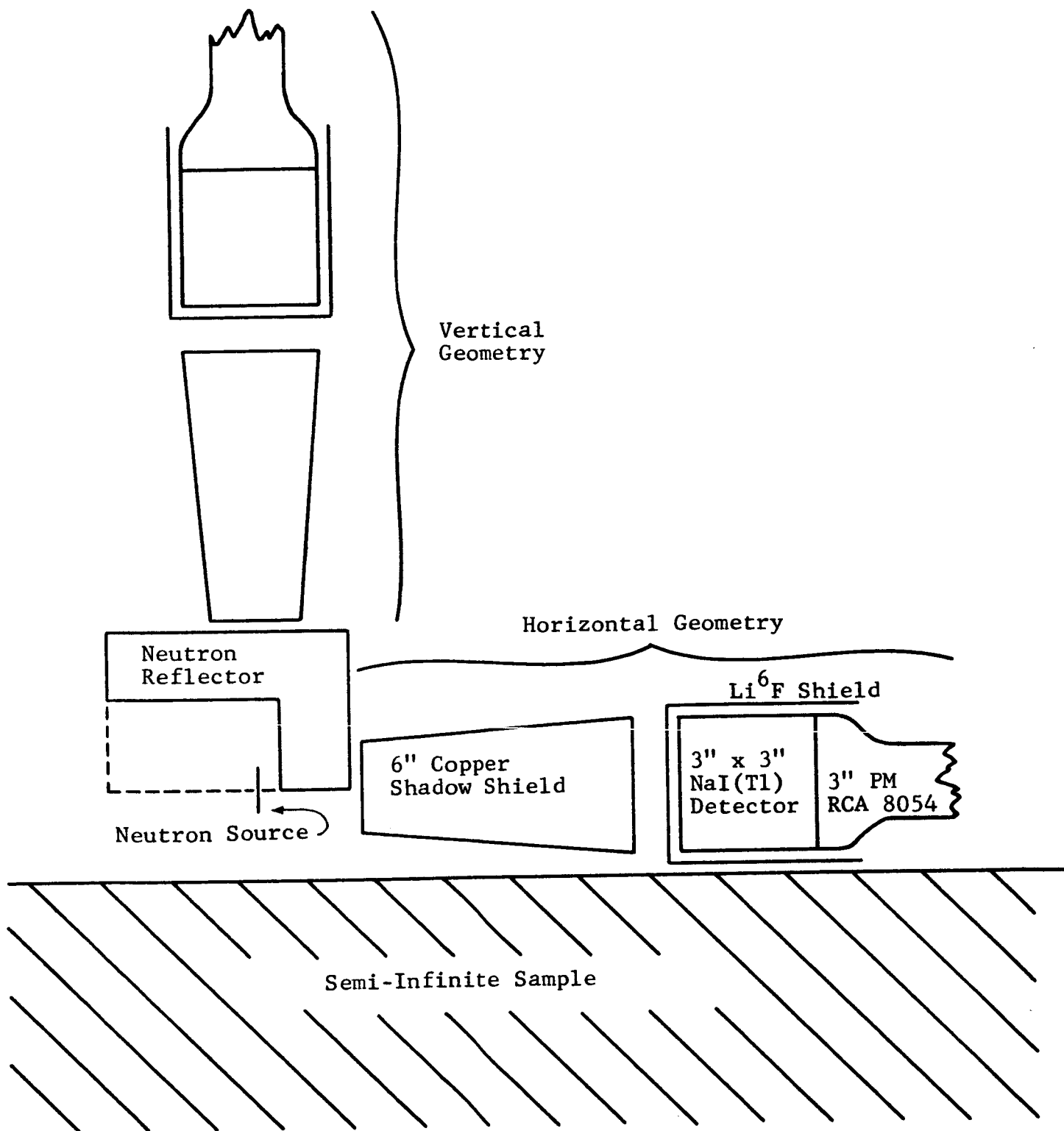


Figure 21

# EXPERIMENTAL CONFIGURATION

Table 8

THE EFFECT OF DETECTOR POSITION ON SPECTRAL RESPONSE  
(500 pps PULSE RATE)

Distance (cm)		Geometry	Thickness of Paraffin Above Source	Relative Fe(n, $\gamma$ ) Intensity (arb. units)	Spectral Quality Index Experimental Theoretical
Source-to-Crystal Crystal-to-Sample					
37	5	Horizontal	8	105	0.30
55					0.28
52	5	Horizontal	8	75	0.20
					---
32	37	Vertical	8	65	0.15
					0.21
47	52	Vertical	8	35	0.10
					0.087
52	5	Horizontal with 4-in. Pb shield	8	70	0.35
					---
27	5	Horizontal (Sandia)	4	140	0.50
					---
27	5	Horizontal (Sandia)	8	300	0.85
					---

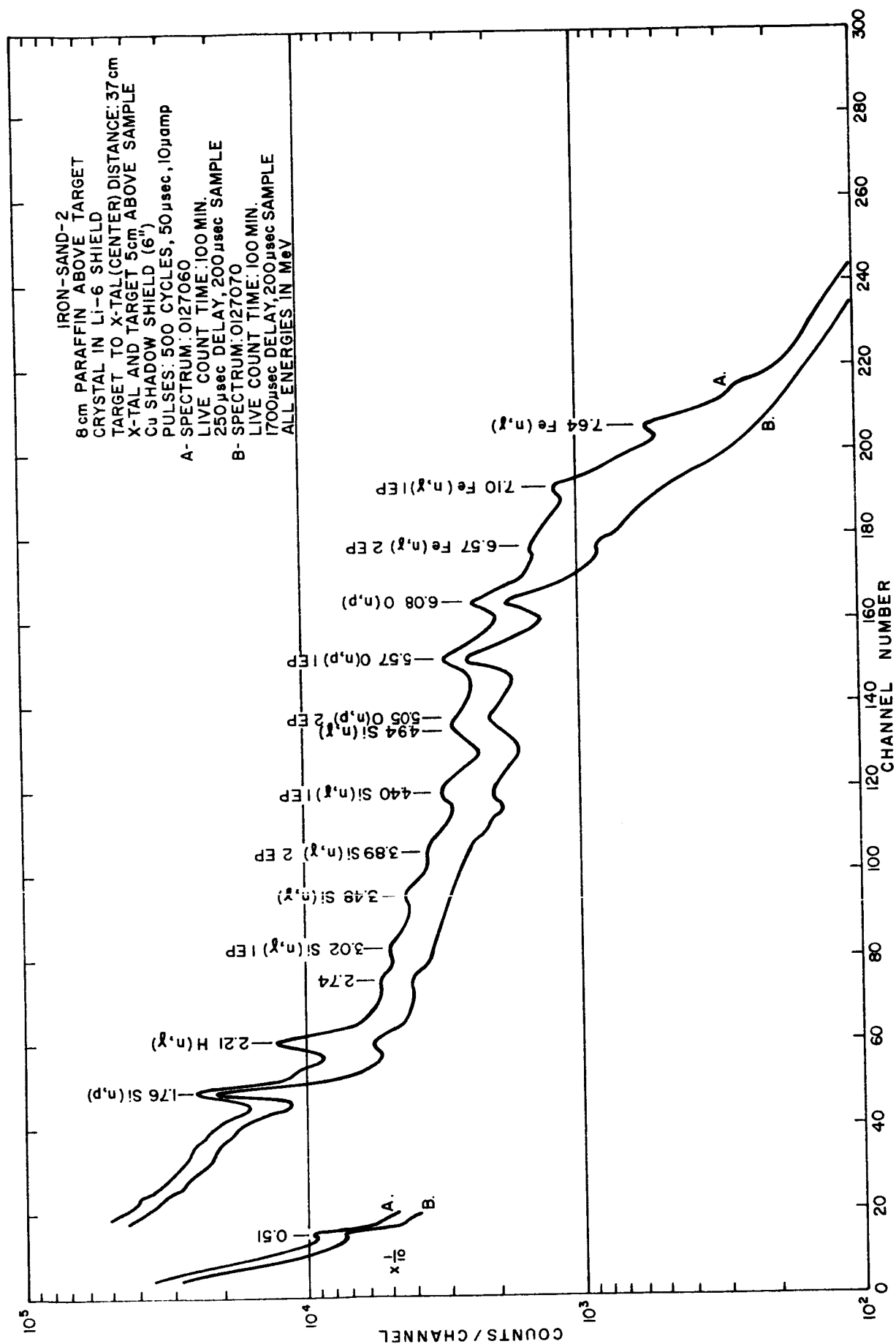


Figure 22

CAPTURE GAMMA-RAY SPECTRUM OF IRON-SAND SAMPLE OBTAINED  
USING HORIZONTAL GEOMETRY WITH 37 cm TARGET TO CRYSTAL DISTANCE

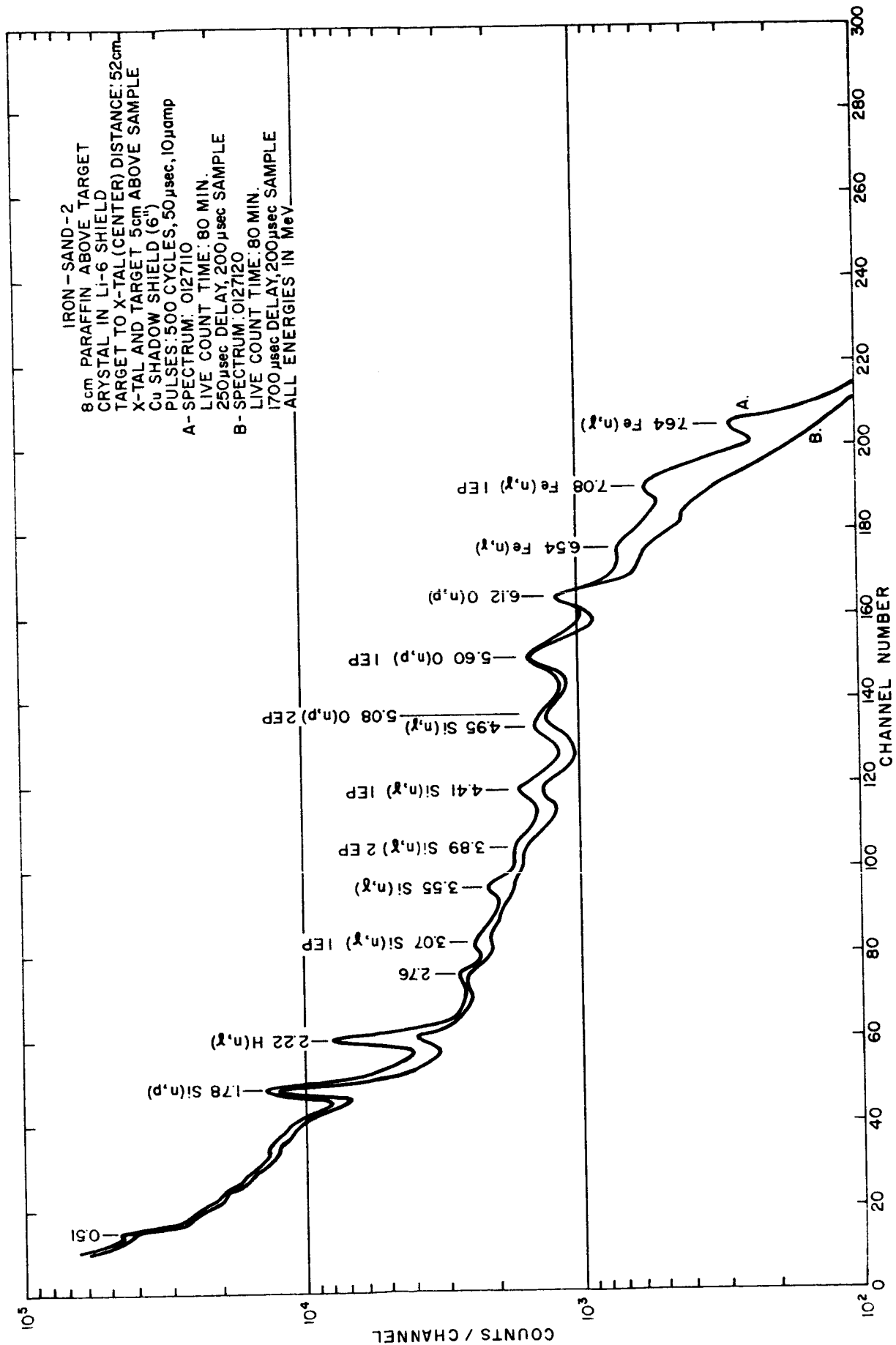


Figure 23  
CAPTURE GAMMA-RAY SPECTRUM OF IRON-SAND SAMPLE OBTAINED USING  
HORIZONTAL GEOMETRY WITH 52cm TARGET TO CRYSTAL DISTANCE

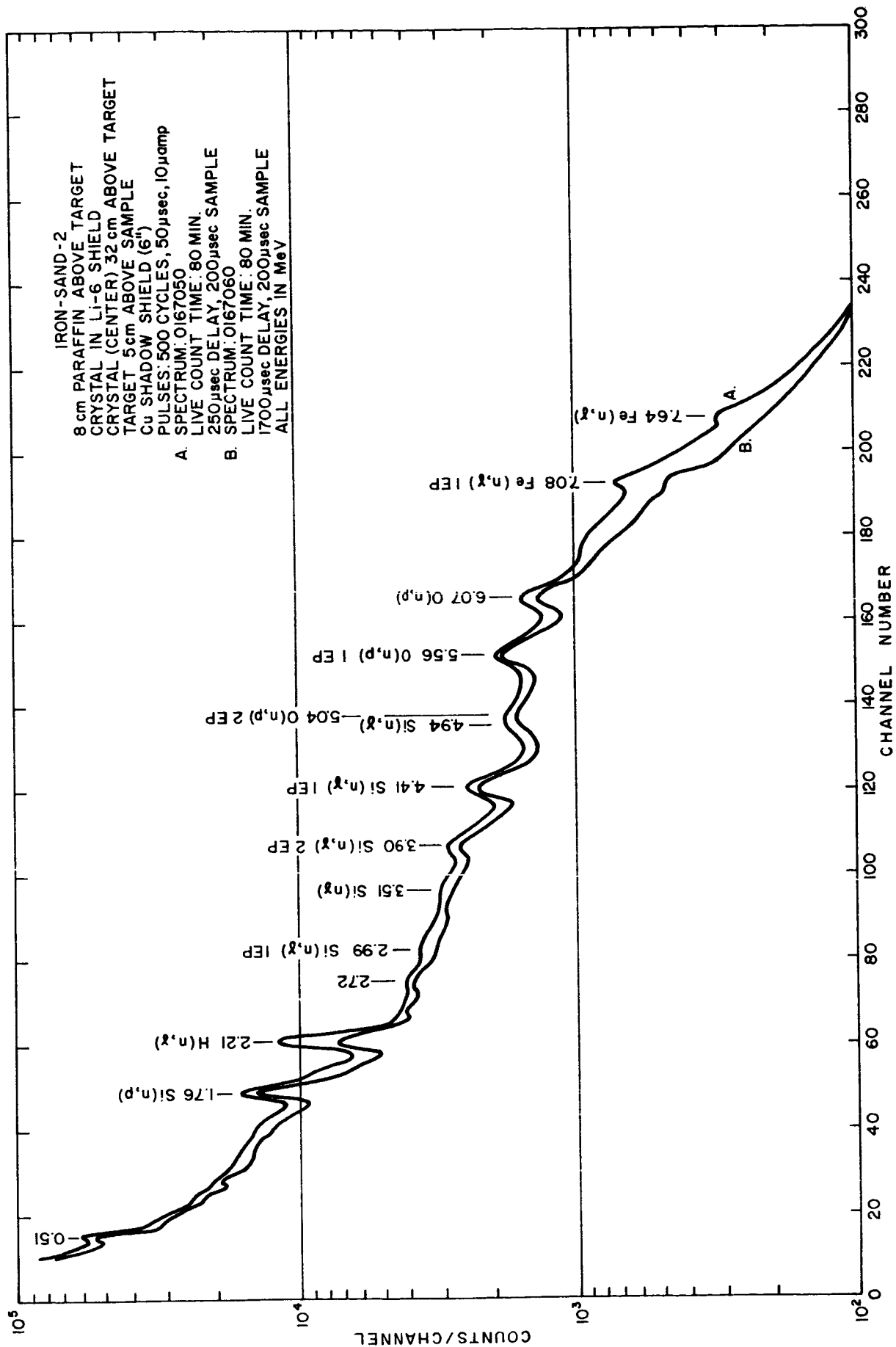


Figure 24  
CAPTURE GAMMA-RAY SPECTRUM OF IRON-SAND SAMPLE OBTAINED USING  
VERTICAL GEOMETRY WITH 32cm TARGET TO CRYSTAL DISTANCE

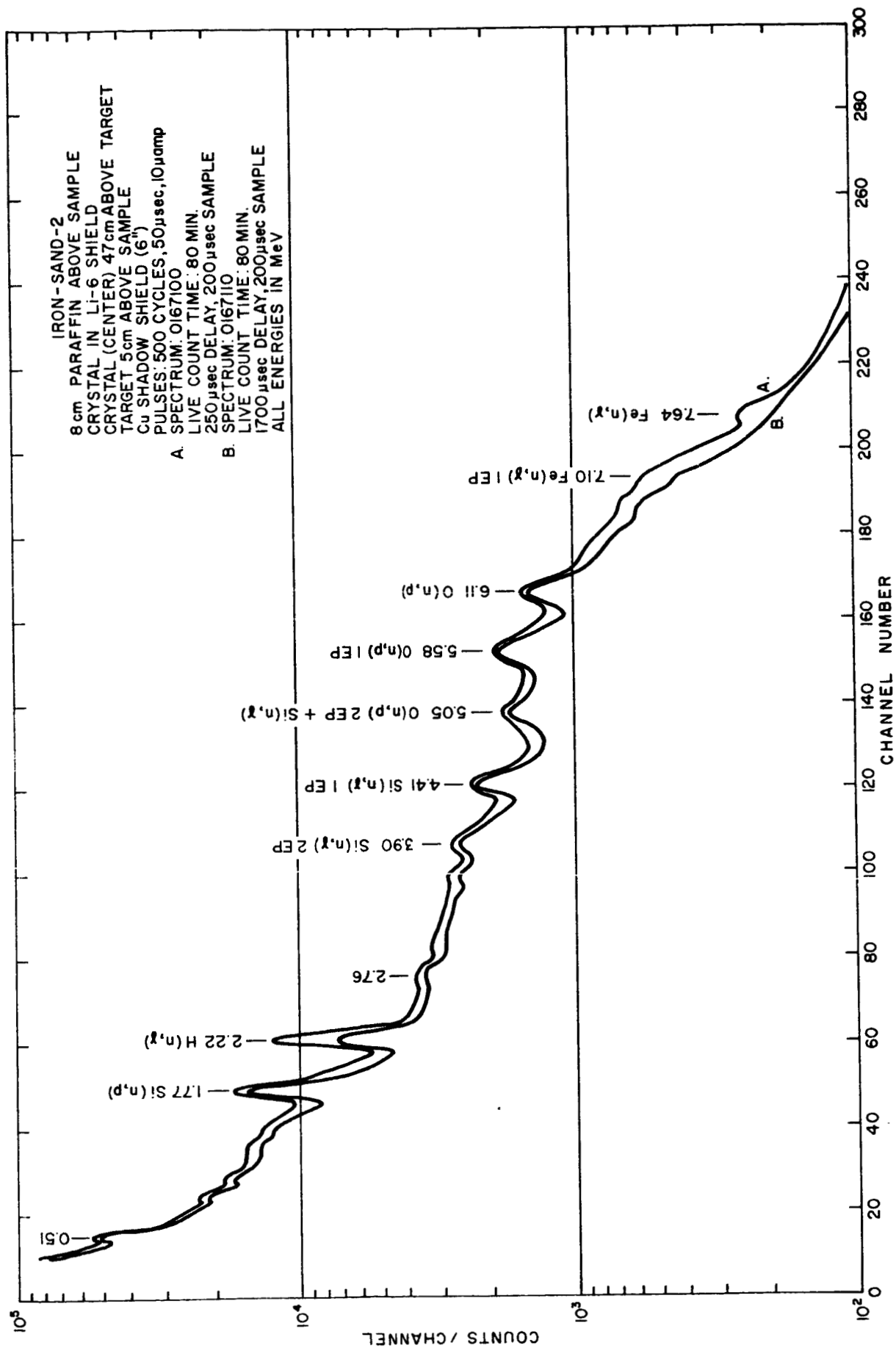


Figure 25  
CAPTURE GAMMA-RAY SPECTRUM OF IRON-SAND SAMPLE OBTAINED USING  
VERTICAL GEOMETRY WITH 47cm TARGET TO CRYSTAL DISTANCE

horizontal geometry is superior to the vertical geometry, and that decreasing the source-to-detector distance increases both the  $\text{Fe}(n,\gamma)$  intensity and the spectral quality index. Theoretical values of the spectral quality index, calculated according to the method of Appendix B, are also listed in Table 8; they give the same results as the experimental measurements.

For the case of horizontal geometry with a source-to-detector distance of 52 cm, a 4-in.-thick lead shield was placed between the source and the shadow shield. The lead shields the detector from the region of the sample directly below the source. The spectrum obtained with this configuration is shown in Figure 26; the relative  $\text{Fe}(n,\gamma)$  intensity and spectral quality index are listed in Table 8. A comparison of the results of the 52-cm horizontal configuration with and without the 4-in. lead shield shows that the addition of the lead shield tends to decrease only slightly the  $\text{Fe}(n,\gamma)$  intensity, while increasing the value of the spectral quality index. This suggests that the active volume for the production of detectable activation gamma rays is located near the source, while the active volume for production of detectable capture gamma rays is located close to the detector. This conclusion is consistent with the theoretical calculations of Appendix B.

The detector-shadow shield-neutron source configuration suggested at the Sandia meeting was also investigated. This is a horizontal geometry configuration employing a 6-in. copper shadow shield with a 2-in. gap between the target and the shadow shield and a 1-in. gap between the shadow shield and the detector. Measurements using this geometry with both 4-cm and 8-cm neutron reflectors were made on the iron-sand-3 sample matrix. The spectra obtained are shown in Figures 27 and 28. As shown by the  $\text{Fe}(n,\gamma)$  intensity and the spectral quality index for these configurations (cf. Table 7), the 27-cm base with a 8-cm neutron reflector produced the best capture gamma-ray spectrum.

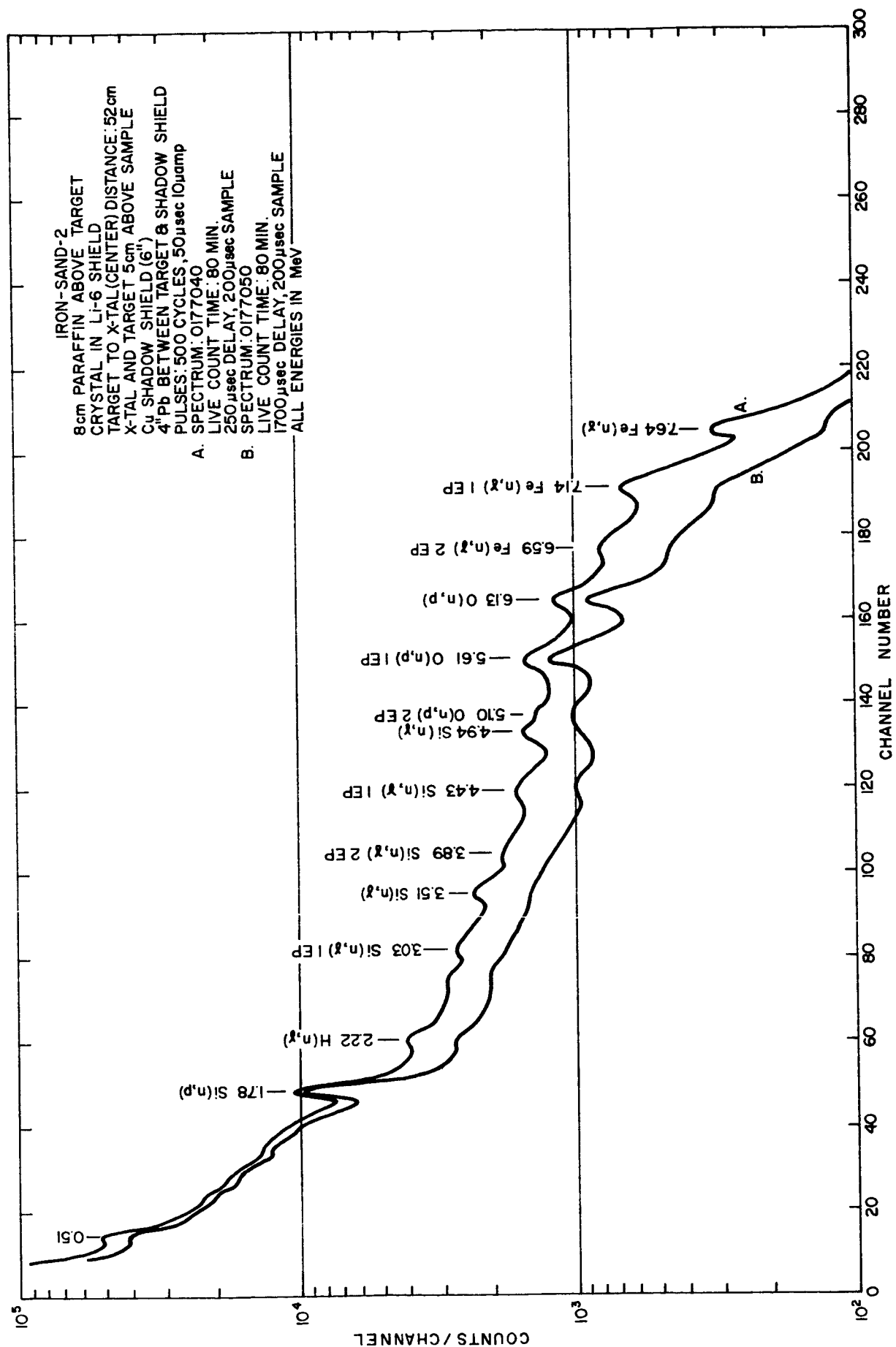


Figure 26  
CAPTURE GAMMA-RAY SPECTRUM OF IRON-SAND SAMPLE OBTAINED USING  
4 in. OF LEAD BETWEEN TARGET AND SHADOW SHIELD

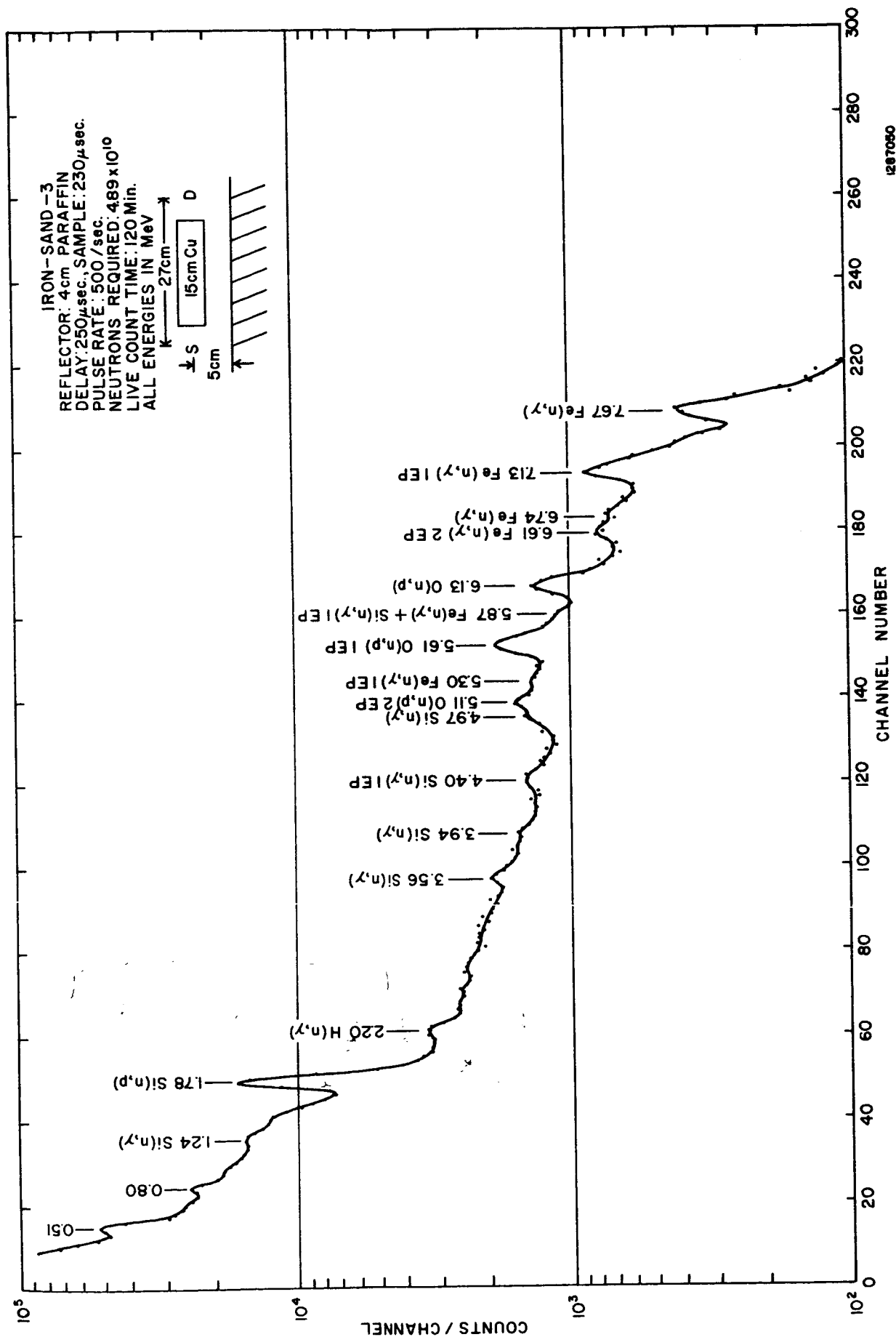


Figure 27  
CAPTURE GAMMA-RAY SPECTRUM OF IRON-SAND SAMPLE OBTAINED USING  
SANDIA GEOMETRY WITH 4cm PARAFFIN ABOVE TARGET

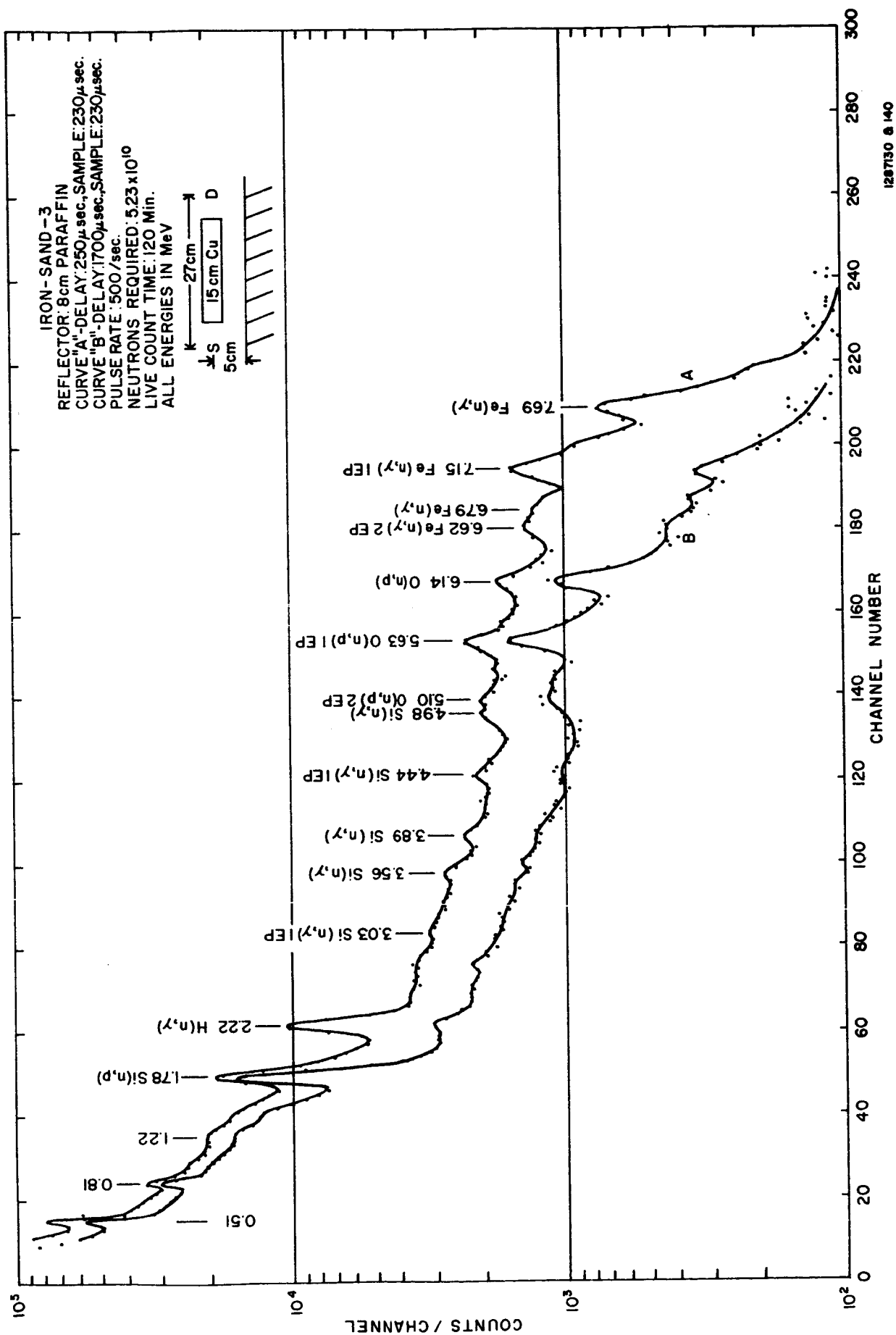


Figure 28  
CAPTURE GAMMA-RAY SPECTRUM OF IRON-SAND SAMPLE OBTAINED USING  
SANDIA GEOMETRY WITH 8cm PARAFFIN ABOVE TARGET

### Addition of Neutron Absorber to Reflector

A reflector located above the neutron source is very beneficial to the capture gamma-ray experiment, as shown by the results in Table 6. However, the reflector is apparently detrimental to the neutron die-away experiment<sup>(8)</sup> because thermal neutrons tend to leak out of the reflector for extended periods of time after the neutron pulse. To decrease this thermal neutron leakage, 0.8 percent boron carbide was added to the 4-cm reflector. This amount of boron carbide increases the thermal neutron capture cross section of the reflector by a factor of ten.

Capture gamma-ray measurements were taken with the iron-sand-3 sample matrix using the 27-cm horizontal geometry and the 4-cm boronated paraffin reflector. The spectrum obtained is shown in Figure 29. Analysis of this spectrum indicates that the relative  $\text{Fe}(n,\gamma)$  intensity is 62 and the spectral quality index is 0.19. Since the same geometry with 4 cm of normal paraffin produced a relative  $\text{Fe}(n,\gamma)$  intensity of 140 and a spectral quality index of 0.48, the addition of a strong thermal neutron absorber to the reflector is clearly detrimental to the capture gamma experiment and is roughly equivalent to the omission of a reflector.

### Neutron Pulse Rate

The analysis performed in Appendix A indicates that the neutron pulse rate strongly affects the quality of the capture gamma-ray data. The ratio of capture gamma-ray count rate to the neutron activation gamma-ray count rate (spectral quality index) was found to vary inversely with the neutron pulse rate. To check this point experimentally, capture gamma-ray measurements were performed with a 1000 pps pulse rate on the iron-sand-3 sample matrix with the 27-cm horizontal geometry and a 4-cm paraffin reflector above the neutron source. The spectrum obtained is shown in Figure 30. For this spectrum,

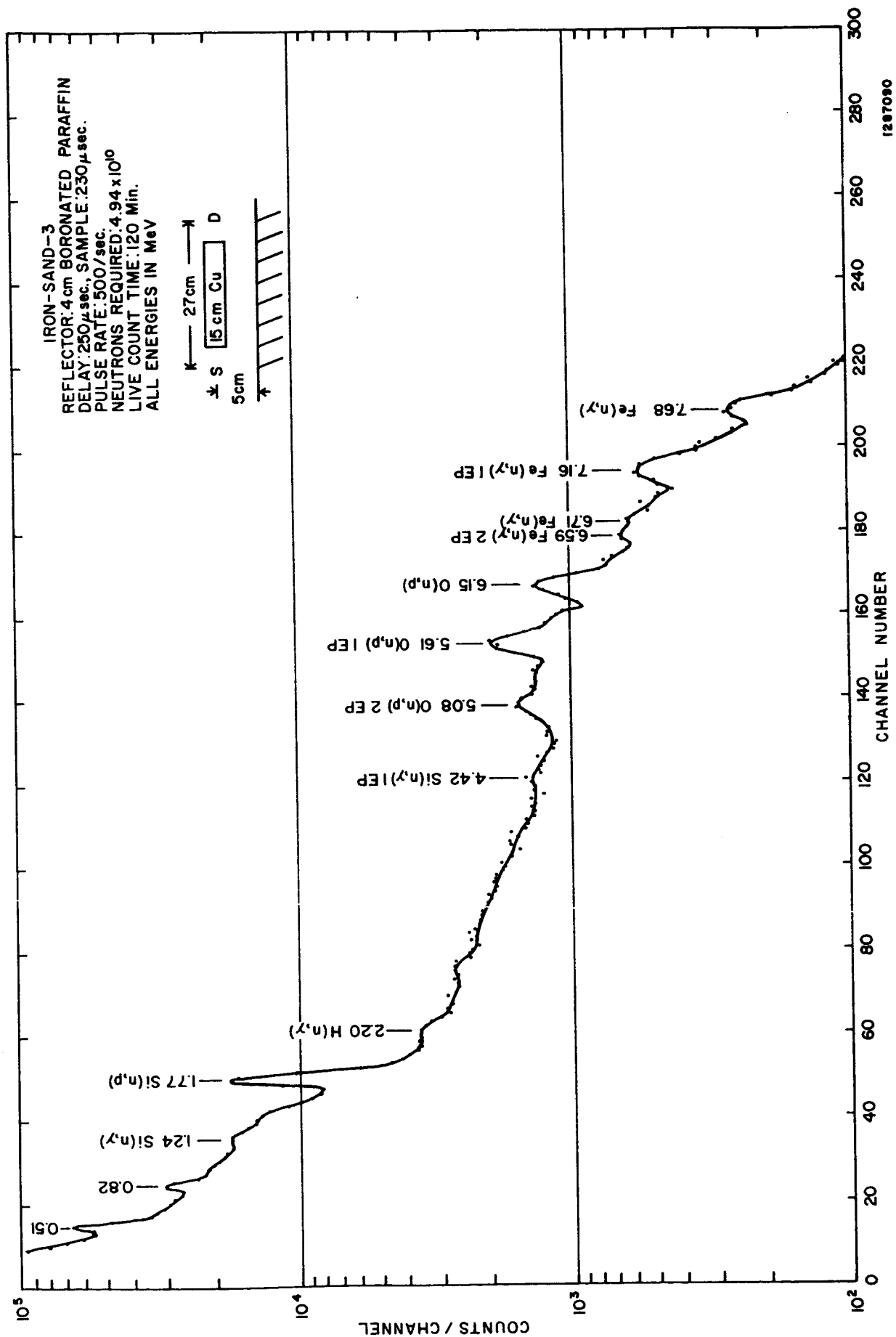


Figure 29  
CAPTURE GAMMA-RAY SPECTRUM OF IRON-SAND SAMPLE OBTAINED USING  
SANDIA GEOMETRY WITH 4cm BORONATED PARAFFIN ABOVE TARGET

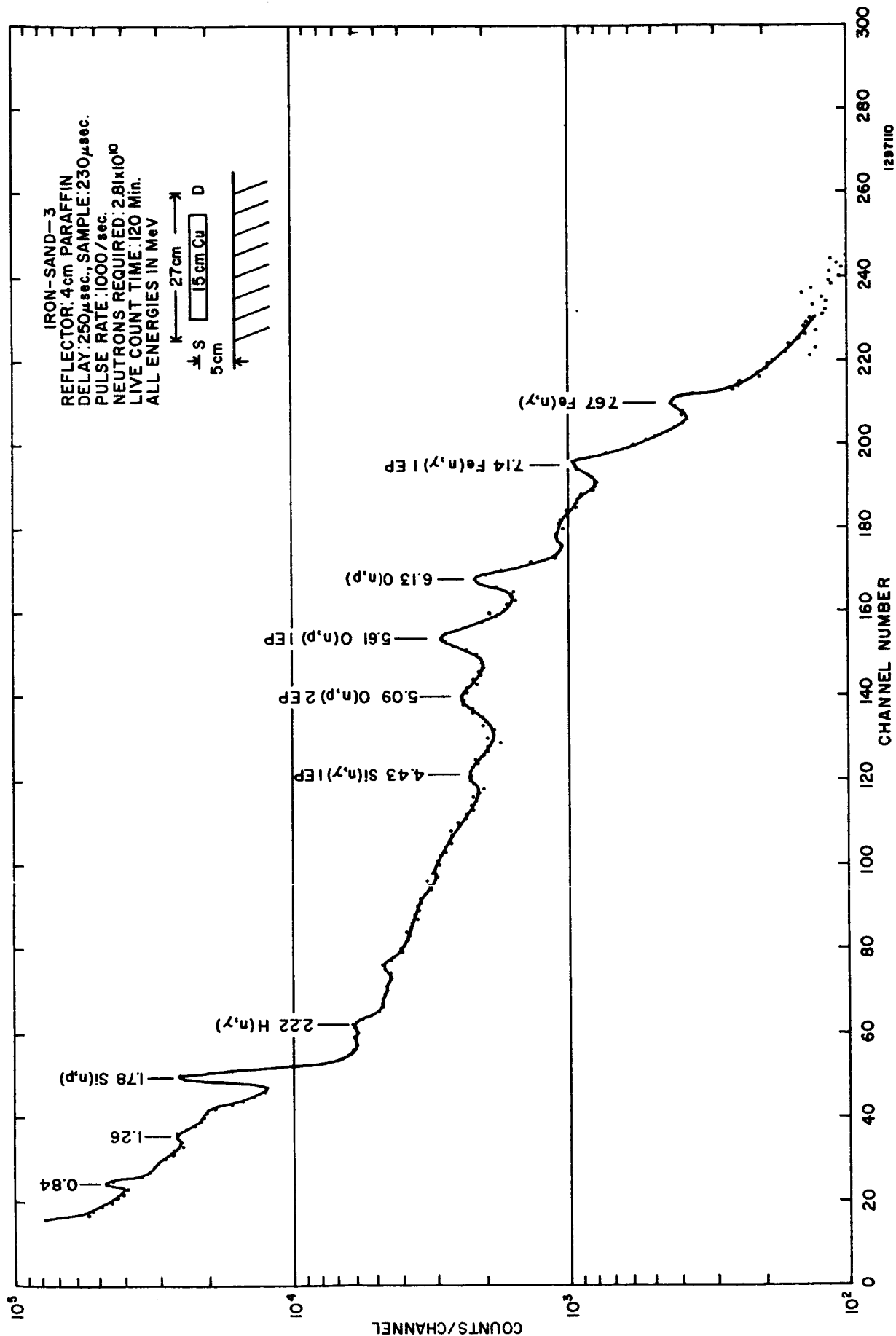


Figure 30  
 CAPTURE GAMMA-RAY SPECTRUM OF IRON-SAND SAMPLE OBTAINED USING  
 SANDIA GEOMETRY WITH 4cm PARAFFIN ABOVE TARGET AND 1000pps PULSE RATE

the spectral quality index was found to be 0.14. Comparison of this result with that obtained using the same geometry and a 500 pps pulse rate (cf. Table 8, Figure 27) indicated the spectral quality index decreased by almost a factor of three. This result tends to support the dependence of the spectral quality of the capture gamma-ray spectrum on the neutron pulse rate.

Comparing Figures 27 and 30 leads to the additional conclusion that the neutrons from the source were not being efficiently utilized. About twice as many counts were recorded in the 1000 pps spectrum (Figure 30) than in the 500 pps spectrum (Figure 27), while fewer neutrons were used in obtaining the 1000 pps spectrum. Also, the number of counts recorded in both of these spectra is about equal to the number of neutron pulses that occurred in the course of obtaining the data. Thus, it appears that the number of counts recorded is proportional to the number of neutron pulses rather than to the number of neutrons used. This appears to result from the fact that, in general, the pulse height analyzer will not handle the signal from more than one or two gamma rays per sampling period, as the duration of each sampling period is only 230  $\mu$ sec and the PHA may require as much as 160  $\mu$ sec to record a pulse. Therefore, additional pulses arriving during the sampling period will be rejected by the PHA and will not be recorded. To use the neutron output from the source efficiently, the number of neutrons per pulse must be reduced to the point where the number of counts recorded is proportional to the number of neutrons used.

### Summary

It was determined that a good quality thermal neutron capture gamma-ray spectrum (Figure 28) can be obtained from a bulk sample using a pulsed 14-MeV neutron source. However, to obtain such a spectrum, the optimization of several parameters had to be considered: the length of sampling

period, the neutron reflector thickness, the detector-source geometry, and the neutron pulse rate.

From theoretical calculations it was determined that, although an optimum sampling period exists (for a given sample and neutron pulse rate), the quality of the capture gamma-ray spectrum is insensitive to the length of the sampling period. Therefore, a sampling period of 250  $\mu$ sec duration, which could be used successfully with neutron pulse rates between 500 pps and 1000 pps, was selected.

The results of both predicted and experimental thermal neutron flux distributions in the sample and the results of capture gamma-ray measurements indicate that a neutron reflector located above the source is very beneficial to capture gamma-ray measurements. However, this reflector is detrimental to the die-away experiment. The addition of 0.8 percent boron carbide to the reflector to make the reflector more nearly compatible with the die-away experiment resulted in the nullification of the benefits of using the reflector.

Horizontal and vertical detector-source geometries were investigated. It was determined both theoretically and experimentally that horizontal geometry with a short source-to-detector distance is the best. It was also found that the active volume for the production of detectable activation gamma rays is located near the source, while the active volume for production of detectable capture gamma rays is located nearer the detector.

Theoretical results indicated that the 500 pps pulse rate should give better capture gamma-ray spectra than the 1000 pps pulse rate. Experimentation supported this prediction.

## CHAPTER VI

### AREAS REQUIRING FURTHER STUDY

While the present study has established the feasibility of applying the capture gamma-ray technique to the analysis of large samples using a 14-MeV pulsed neutron source, there remain several areas related to the optimization and expected sensitivity of the capture gamma-ray experiment, especially in conjunction with the other experiments, that will require further investigation.

The studies discussed in the preceding sections were conducted using a nonhomogeneous iron-sand sample. While this sample was probably adequate for determining the effect that several of the experimental parameters may have on the recorded spectrum, it is impossible to determine the ability of the technique to measure the relative concentrations of elements other than iron, silicon, and oxygen with this sample. Large samples of several rock types (such as granite and basalt) will be required to provide a means to determine experimentally the sensitivity of the capture experiment (cyclic activation can also be studied).

In the preceding studies, the number of neutrons produced by the Van de Graaff during each pulse was much larger than optimum for the capture gamma-ray experiment. This resulted in the inefficient use of the neutrons as well as possible degradation of the capture gamma-ray spectrum. As discussed in Appendix A, the gamma-ray detector requires about 200  $\mu$ sec after a neutron burst to recover and operate properly. It is likely that, if the number of neutrons per pulse is reduced substantially, this overloading of the detector system could be greatly reduced, if not eliminated entirely. Experimentation is required to establish the optimum number of neutrons that should be produced per neutron burst and the effect that this

change would have on the resulting capture gamma-ray spectrum. (Presently it is expected that about  $1 \times 10^3$  neutrons per pulse would be acceptable.)

The use of a neutron reflecting material, such as paraffin, placed above the neutron source has been found to increase greatly the sensitivity of the capture gamma-ray experiment. This is accomplished by increasing the low-energy neutron flux near the surface without perturbing the fast neutron flux ( $> 11$  MeV). Such a reflector apparently does not interfere with either the neutron inelastic scatter experiment or the activation analysis experiment. However, the presence of low-Z material in the vicinity of the target would make the measurement of the epithermal die-away in the sample very difficult, if not impossible.<sup>(8)</sup> This interference will require more study by both participating investigators to determine methods by which this problem can be circumvented. At present, the position which IITRI assumes is that, while the presence of this reflector is not absolutely essential to the capture gamma-ray experiment, it is highly desirable.

There are a number of other experimental parameters that can affect the sensitivity of the capture gamma-ray experiment. The investigators concerned with the individual experiments and the engineers concerned with the hardware for the combined experiment must come to an agreement on several critical items before a meaningful estimate of the sensitivity (in the combined experiment configuration) can be made for any of the individual experiments.

It is felt that resolution of the following parameters is a necessary prerequisite to further experimental investigation regarding total combined experiment capability and sensitivity.

1. Experimental Configuration:

- a. Distance between detector and neutron source;
- b. Height of source and detector above sample surface;

- c. Amounts, types, and positions of neutron shielding (thermal and fast);
- d. Amounts, types, and configurations of support structures required for integration of the several experiments.

2. Hardware Characteristics:

- a. Neutron generator - pulses per second, neutrons per pulse, pulse duration, pulse timing signal;
- b. Pulse height analyzer - dead time, pulse routing capabilities, stability;
- c. Detector resolution;
- d. Amplifier and preamplifier - overload characteristics, recovery time, stability.

3. Data Collection:

- a. Time-sharing feasibility of the pulse height analyzer;
- b. Number of neutrons available for each experiment

If agreement concerning these experimental parameters is reached and the studies mentioned above are completed, it is felt that the sensitivity of the capture gamma-ray technique can be determined and the feasibility of the combined neutron experiment can be established with confidence.

## REFERENCES

1. R. L. Caldwell, W. R. Mills, Jr., L. S. Allen, P. R. Bell and R. L. Heath, *Science* 152 (1966) 457.
2. A. P. Vinogradov, Yu. A. Surkov and G. M. Chernov, *Doklady Akademii Nauk SSR* 170 (1966) 561.
3. H. V. Argo, R. F. Taschek, H. M. Agnew, A. Hemmendinger and W. T. Leland, *Phys. Rev.* 87 (1952) 612.
4. S. J. Bame, Jr. and J. E. Perry, Jr., *Phys. Rev.* 107 (1957) 1616.
5. B. G. Carlson, Atomic Energy Commission Report, La-1891 (1955)
6. Proceedings of the 1965 International Conference on Modern Trends in Activation Analysis, April 19-22, 388.
7. R. C. Greenwood and J. H. Reed, IIT Research Institute Report, IITRI-1193-35.
8. R. L. Caldwell and W. R. Mills, Jr., Private Communication.

## APPENDIX A

### OPTIMUM SAMPLING PERIOD

When using a pulsed source of neutrons, the intensity of the capture gamma rays emitted from a sample will decrease as a function of time after the neutron pulse. The rate of this decrease in intensity depends on the thermal neutron lifetime in the sample. However, the intensity of the natural background will remain constant with time. Also, if the time between neutron pulses is short compared to the half-life of any radionuclide produced by activation, this induced radioactivity will quickly reach a state of equilibrium and will thereafter remain approximately constant. This is the case encountered when using a pulsed 14-MeV neutron source for capture gamma-ray analysis of a geological sample, i.e., the background is constant with time since it is due primarily to the decay of  $N^{16}$  (7.35 sec half-life). Therefore, it should be possible to optimize the duration of the sampling period so that the fractional error in the observed capture gamma-ray signal is minimum. The derivation of an expression for this optimum sampling period and a discussion of its application to the experimental cases follow.

Assume that the analyzer is gated on for a time interval  $t$  beginning at a predetermined time after the neutron pulse (the beginning of the interval being determined by the time required to let the detector recover from the neutron pulse). Then the counts observed during the sampling period will be

$$C = N_0 \tau (1 - e^{-t/\tau}) + Bt, \quad (A-1)$$

where  $N_0$  is the signal count rate at time zero,  $B$  is the background count rate (in the same energy region as the signal) which is assumed to be constant, and  $\tau$  is the mean lifetime of

the thermal neutrons in the sample. The observed signal,  $S$ , is

$$S = N_0 \tau (1 - e^{-t/\tau}). \quad (\text{A-2})$$

The error in  $S$  is  $(C + Bt)^{1/2}$  and the fractional error in  $S$  is  $(C + Bt)^{1/2}/S$ . It can be shown that the fractional error in  $S$  is a minimum when the following equation is satisfied:

$$e^{t/\tau} - 1 = \frac{1}{2} \frac{N_0}{B} (1 - e^{-t/\tau}) + \frac{2t}{\tau}. \quad (\text{A-3})$$

The minimization of the fractional error in  $S$  is used as the criterion for the optimization of the counting period.

The optimum sampling period,  $t$ , can be determined as a function of the signal-to-noise ratio,  $N_0/B$ . As examples, consider the two cases where  $\tau = 282 \mu\text{sec}$  and  $\tau = 155 \mu\text{sec}$ . The results, given in Figure A-1, show that  $N_0/B$  is a finite positive number only for a small range of sample periods. Therefore, the minimization of the fractional error for all possible signal-to-noise ratios can be accomplished only within this small range of sample periods.

Consider the four cases which were investigated experimentally: (a)  $\tau = 282 \mu\text{sec}$ , 500 pps pulse rate; (b)  $\tau = 155 \mu\text{sec}$ , 500 pps pulse rate; (c)  $\tau = 282 \mu\text{sec}$ , 1000 pps pulse rate; (d)  $\tau = 155 \mu\text{sec}$ , 1000 pps pulse rate. The signal-to-noise ratio,  $N_0/B$ , was measured to be approximately two for cases (a) and (b) (500 pps pulse rate). This was done by obtaining the ratio of the number of counts in the 7.64 MeV  $\text{Fe}(n, \gamma)$  peak during the period 250 to 300  $\mu\text{sec}$  after the neutron pulse to the number of counts in the same energy region during the period 1900 to 1950  $\mu\text{sec}$  after the neutron pulse.

In the capture gamma-ray experiment using a pulsed 14-MeV neutron source, the capture gamma ray count rate per second,

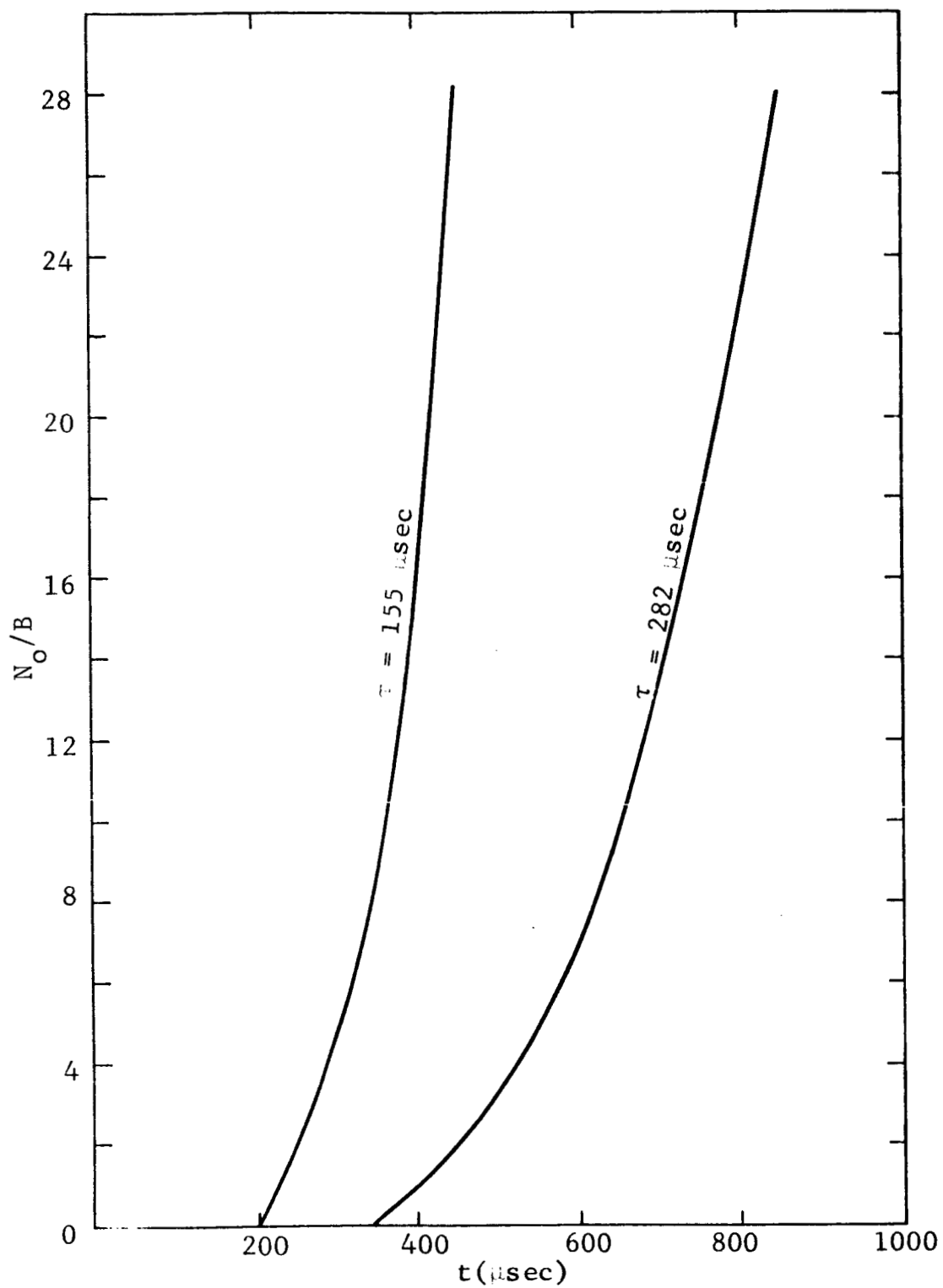


Figure A-1  
OPTIMUM SAMPLE DURATION AS A FUNCTION OF  $N_o/B$

$R_\gamma$ , will be

$$R_\gamma = K_\gamma n f, \quad (\text{A-4})$$

where  $K_\gamma$  is a constant,  $n$  is the neutron output per pulse, and  $f$  is the pulse rate.  $R_b$ , the background count rate per second from the decay of  $N^{16}$ , will be

$$R_b = K_b \phi f, \quad (\text{A-5})$$

where  $K_b$  is a constant and  $\phi$  is the average 14-MeV neutron flux seen by the sample during several  $N^{16}$  half-lives. Since  $\phi \propto n f$ ,

$$R_b = K'_b n f^2, \quad (\text{A-6})$$

where  $K'_b$  is another constant. Thus,  $R_b$  varies with the square of the pulse rate (for a constant number of neutrons per pulse), as both the sampling rate and the  $N^{16}$  level are proportional to the pulse repetition rate. The signal-to-noise ratio will be, therefore,

$$\frac{N_o}{B} = \frac{R_\gamma}{R_b} = \frac{K_\gamma}{K'_b f} = \frac{K}{f}, \quad (\text{A-7})$$

where  $K = K_\gamma / K'_b$ . Equation (A-7) shows that the signal-to-noise ratio is inversely proportional to the pulse rate and is independent of the number of neutrons per pulse. For cases (c) and (d) (1000 pps pulse rate), then,  $N_o/B$  will be assumed to be unity.

From equation (A-3) and the above values for  $N_o/B$  the optimum sampling times for the four cases were found to be

<u>Case</u>	<u>Optimum t</u>
a	450 $\mu$ sec
b	250 $\mu$ sec
c	410 $\mu$ sec
d	255 $\mu$ sec.

Therefore, the optimum length of the sampling period is sensitive to the thermal neutron lifetime.

Since in lunar and planetary applications both the thermal neutron lifetime in the sample and the signal-to-noise ratio will be unknown, the sensitivity of the fractional error in the observed signal,  $S$ , as a function of  $t$  and  $N_0/B$  must be determined. The results for the four cases are:

Case (a)  $\tau = 282 \mu$ sec,  $N_0/B = 2$  (500 pps pulse rate)

<u>t</u>	<u>Fractional Error in S</u>
250 $\mu$ sec	86.9 $B^{-1/2}$
450 $\mu$ sec (Optimum)	81.7 $B^{-1/2}$
500 $\mu$ sec	81.8 $B^{-1/2}$

Case (b)  $\tau = 155 \mu$ sec,  $N_0/B = 2$  (500 pps pulse rate)

<u>t</u>	<u>Fractional Error in S</u>
200 $\mu$ sec	111 $B^{-1/2}$
250 $\mu$ sec (Optimum)	110 $B^{-1/2}$
300 $\mu$ sec	111 $B^{-1/2}$

Case (c)  $\tau = 282 \mu$ sec,  $N_0/B = 1$  (1000 pps pulse rate)

<u>t</u>	<u>Fractional Error in S</u>
250 $\mu$ sec	155 $B^{-1/2}$
410 $\mu$ sec (Optimum)	149 $B^{-1/2}$
500 $\mu$ sec	150 $B^{-1/2}$

Case (d)  $\tau = 155 \mu\text{sec}$ ,  $N_0/B = 1$  (1000 pps pulse rate)

<u>t</u>	<u>Fractional Error in S</u>
150 $\mu\text{sec}$	207 $B^{-1/2}$
225 $\mu\text{sec}$ (Optimum)	201 $B^{-1/2}$
300 $\mu\text{sec}$	204 $B^{-1/2}$

Therefore, although an optimum length for the sampling period exists, the fractional error in S is quite insensitive to it. Consider the sensitivity of the fractional error in S as a function of  $N_0/B$ . For signal-to-noise ratios of 0.15, 2, and 4.8 the fractional errors in S were calculated for  $t = 250 \mu\text{sec}$  and compared to the results for optimum t (for each value of  $N_0/B$ ). The value  $\tau = 155 \mu\text{sec}$  was assumed in these calculations. The results are

<u><math>N_0/B</math></u>	<u>Fractional Error in S</u>	
	<u>t = 250 <math>\mu\text{sec}</math></u>	<u>Optimum t</u>
0.15	1220 $B^{-1/2}$	1210 $B^{-1/2}$
2	110 $B^{-1/2}$	110 $B^{-1/2}$
5	55.6 $B^{-1/2}$	55.3 $B^{-1/2}$

These results show that, although the fractional error in S varies strongly with  $N_0/B$ , the sampling period is not critical, i.e., for a given  $N_0/B$  the fractional error in S is quite insensitive to the sampling period.

The above results are important, since in lunar and planetary applications the thermal neutron lifetime,  $\tau$ , and the signal-to-noise ratio,  $N_0/B$ , are unknown quantities.

For experimental investigations of the iron-sand sample the length of the sampling period was initially chosen (when  $\tau = 282 \mu\text{sec}$ ) to be 200  $\mu\text{sec}$ . This duration was selected because it could be used conveniently with both the 500 pps and 1000 pps pulse rates. Subsequently, when the analyzer sequence switch was available, the length of the sampling period was changed to 230  $\mu\text{sec}$ . This was done because a capacitor

yielding this duration was available, while none was available giving a duration of 250  $\mu$ sec. However, the length of the sampling period has been shown not to be critical

If one compares the fractional error in S for each of the four cases using  $t = 250 \mu$ sec,  $B_o$  for the background in the 500 pps pulse rate cases, and  $2B_o$  for the background in the 1000 pps pulse rate cases (for a given sample and given neutron output per pulse, the background with a 1000 pps pulse rate will be twice that for a 500 pps pulse rate), the following results are obtained:

Case (with $t = 250 \mu$ sec)	Fractional Error in S
a	$86.9 B_o^{-1/2}$
b	$110 B_o^{-1/2}$
c	$110 B_o^{-1/2}$
d	$143 B_o^{-1/2}$

Thus, for both values of the thermal neutron lifetime the fractional error in S with the 500 pps pulse rate is about 20 percent lower than with the 1000 pps pulse rate.

In the actual experiment, a true measurement of the background cannot be obtained. Rather one gets a set of counts

$$C_s = N_o \tau (1 - e^{-t/\tau}) + Bt \quad (A-8)$$

during the counting period immediately following the neutron pulse and a second set of counts

$$C_b = N_o \tau e^{-r/\tau} (e^{t/\tau} - 1) + Bt \quad (A-9)$$

during the "background" counting period, where r is the time of the end of the "background" sampling period. Unless Bt can be measured independently by counting for a significant

period of time after the end of a neutron pulse, one must work with the quantity

$$S' = C_s - C_b \quad (A-10)$$

which is related to the desired signal S by the expression

$$S' = S(1 - e^{-\frac{r-t}{\tau}}). \quad (A-11)$$

If the fractional error in S' is optimized in the same manner as for S in order to see what gain can be made by background subtraction, the following optimum sampling times for our four cases are obtained

<u>Case</u>	<u>Optimum t</u>
a	440 $\mu$ sec
b	250 $\mu$ sec
c	240 $\mu$ sec
d	200 $\mu$ sec

Here a delay time of 250  $\mu$ sec has been assumed so that  $r = 1750$   $\mu$ sec for cases a and c and  $r = 750$   $\mu$ sec for cases b and d. Not only are these optimum times close to the corresponding times for the case without background subtraction, but the fractional errors in S' are very close to those in S. The same situation as before holds with regard to pulse rate variation. From equation (A-7) it is seen that the spectral quality index (the ratio of the capture gamma-ray count rate to the neutron activation count rate) varies inversely with the pulse rate. Hence, the spectral quality index for the 500 pps pulse rate is twice that for the 1000 pps pulse rate.

Conclusions to be drawn from the above results are:

- (1) in general, the fractional error in the observed signal is unaffected by background subtraction;
- (2) for a given sample,

pulse rate, and configuration, the fractional error in the observed signal is relatively insensitive to the length of the counting period; (3) the spectral quality index is higher and the fractional error in the observed signal is lower for the 500 pps pulse rate. Therefore, prior knowledge of the thermal neutron lifetime in the sample and the signal-to-noise ratio is not necessary for the determination of the length of the sampling period.

## APPENDIX B

### ORIGIN OF THE THERMAL NEUTRON CAPTURE AND FAST NEUTRON INDUCED GAMMA RAYS

The optimum experimental configuration used to detect and measure the capture gamma-rays is dependent on the location of the active volume in the sample. (Active volume means the volume from which the bulk of the gamma rays that reach the detector position originate.) Therefore, a series of calculations was undertaken to determine the active volume for both the capture gamma rays and the gamma radiation which results from fast neutron activation of the sample.

#### Procedure

Once the neutron flux distribution is known, it is possible to estimate the contribution,  $\phi_{ij}$ , of each segment of the sample to the total gamma-ray flux observed at the detector position. Let us consider the contribution of one such segment. If we assume that the neutron flux is constant throughout the segment and that the dimensions of the segment are small by comparison to the distance to the detector position,

$$\phi_{ij} = \frac{N_j K_j V_i \rho_i N_o \sigma_j f_{ij}}{A 4\pi R_i^2} \exp \left[ -(\Sigma(E)) \rho S_i \right] \quad (B-1)$$

where

the  $i^{th}$  index refers to the  $i^{th}$  segment

$j = 1$  refers to thermal neutron capture

$j = 2$  refers to fast neutron activation

$\phi_{ij}$  = contribution to the gamma flux at the detector location due to the  $i^{th}$  segment ( $\gamma$ 's/cm<sup>2</sup>sec)

$V_i$  = volume of the  $i^{th}$  segment (cm<sup>3</sup>)

- $f_{ij}$  = neutron flux in the  $i^{\text{th}}$  segment ( $\text{n/cm}^2\text{sec}$ )  
 $R_i$  = distance from the centroid of the segment to the detector position (cm)  
 $S_i$  = straight-line distance through the sample from the  $i^{\text{th}}$  segment to the detector position (cm)  
 $\sigma_j$  = appropriate neutron cross section ( $\text{cm}^2/\text{atom}$ )  
 $\Sigma(E)$  = attenuation coefficient for gamma rays of energy  $E$  in the sample material ( $\text{cm}^2/\text{gm}$ )  
 $K_j$  = intensity of the gamma ray of interest ( $\gamma$ 's/n-interaction)  
 $\rho$  = density of the sample ( $\text{gm/cm}^3$ )  
 $A$  = atomic weight of the sample ( $\text{gm/gm}\cdot\text{mole}$ )  
 $N_o$  = Avogadro's number ( $\text{molecules/gm}\cdot\text{mole}$ )  
 $N_j$  = number of atoms of interest per sample molecule (atoms/molecule)

The  $\phi_{ij}$ 's have been evaluated for the following specific cases: (1) neutron source located 15 cm above the surface with the detector located 15 cm above the surface and 40 cm from the neutron source, and (2) neutron source located 5 cm above the surface with the detector located in several different positions. In all cases, the calculations were performed for thermal neutron capture in silicon and 14-MeV neutron activation of oxygen.

#### Source 15 cm Above Surface

On the basis of the thermal neutron flux distribution measured with a 4-cm paraffin reflector and reported in Figure 9, calculations were performed to determine the active volume for thermal neutron capture. In a sand sample, only silicon will contribute to the capture gamma-ray spectrum, since the thermal capture cross section for oxygen is extremely small. The capture gamma-ray spectrum of silicon is presented in Figure 15.

With the following values for the parameters

$$\begin{array}{ll} \sigma_1 = 80 \times 10^{-27} \text{ cm}^2, & \Sigma = 0.0316 \text{ cm}^2/\text{gm at } E = 4 \text{ MeV}, \\ K \sim 0.5 \text{ } \gamma/\text{interaction}, & \gamma = 1.74 \text{ gm/cm}^3, \\ A = 60 \text{ gm/gm}\cdot\text{mole}, & N_1 = 1 \text{ atom/molecule}, \end{array}$$

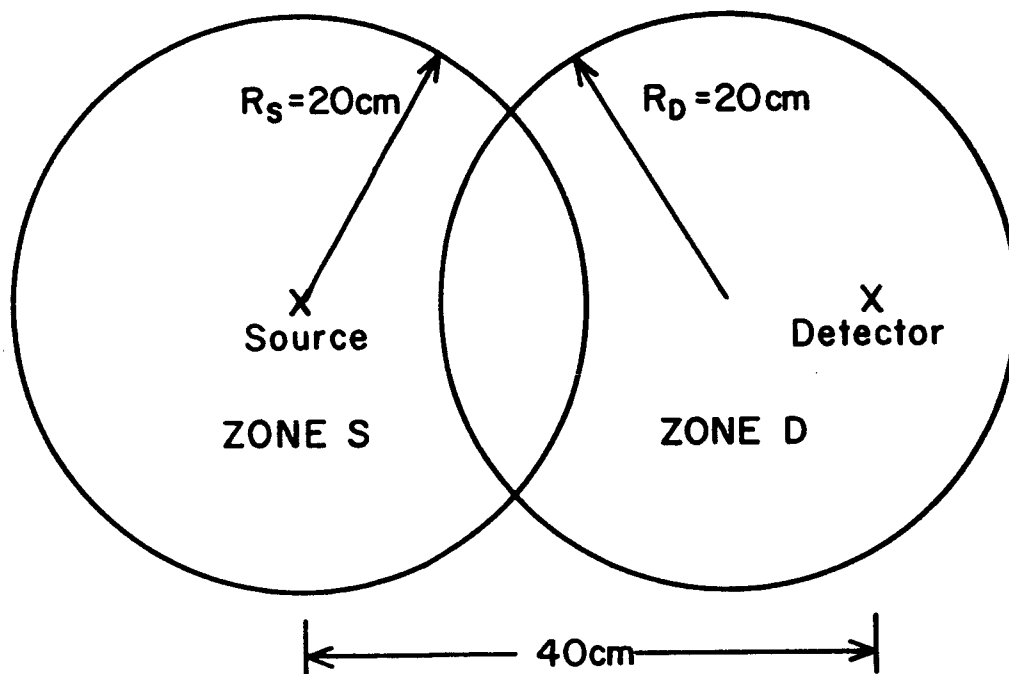
equation (B-1) becomes

$$\phi_{i1} = 5.55 \times 10^{-5} \frac{V_i f_{i1}}{R_1^2} \exp \left[ -0.055 S_i \right] . \quad (\text{B-2})$$

The evaluation of equation (B-2) for each of more than one hundred segments leads to the result that 87 percent of the capture gamma rays that reach the detector position originate in the top 20 cm of the sample and 11 percent originate in the layer 20 to 40 cm below the surface.

Further insight into where the capture gamma rays originate may be gained by considering the two Zones S and D, indicated in Figure B-1. Zone S includes that volume of sample enclosed by a cylinder centered directly below the neutron source having a 20 cm radius and a 20 cm thickness. Zone D encloses a volume of sample identical to that of Zone S but centered 10 cm horizontally from a point directly below the detector position and in the direction of the neutron source. Zone D is found to contribute about 40 percent of the total capture gamma-ray flux while Zone S contributes only 22 percent. Thus the active volume for the capture gamma rays includes a relatively small area of the sample directly below the detector and a depth of about 20 cm.

The origin of the 14-MeV neutron-induced activity is the fast neutron activation of oxygen via the  $O^{16}(n,p)N^{16}$  reaction. This reaction is potentially a source of interference because of the high energy gamma rays associated with it (6.13 MeV and 7.12 MeV). Therefore, it is of interest to determine the active volume associated with this reaction.



( Zone S and D are both 20cm thick)

Figure B-1  
THE RELATIVE LOCATION OF ZONE S AND ZONE D

While the 14-MeV neutron flux distribution was not measured within the sand sample, a first order approximation to the distribution can be made by assuming the functional dependence

$$f_{i2} = \frac{C}{r_i^2} \exp \left[ -\lambda \ell_i \right], \quad (\text{B-3})$$

where

- C = proportionality constant,
- $r_i$  = distance from the neutron source to the point of interest (cm),
- $\ell_i$  = straight-line distance through sand between the point of origin of the neutron and the point of interest (cm)
- $\lambda$  = 14-MeV neutron removal coefficient ( $\text{cm}^{-1}$ ).

The proportionality constant C can be evaluated using the 14-MeV result presented in Figure 9.

$$(f_2) = 2.1 \times 10^5 \text{ n/cm}^2 \text{ sec} \\ \text{at } r = 15 \text{ cm and } \ell = 0.$$

Therefore,  $C = 4.7 \times 10^7$ .

The 14-MeV neutron removal coefficient of the sand sample was measured using copper foils placed at several depths below the surface of the sand and was found to be approximately  $0.05 \text{ cm}^{-1}$ . Equation (B-3) then becomes

$$f_{i2} = \frac{4.7 \times 10^7}{r^2} \exp \left[ -0.05 \ell_i \right]. \quad (\text{B-4})$$

Equation (B-1) may now be written assuming

$$\begin{array}{ll} \sigma_2 = 42 \times 10^{-27} \text{ cm}^2 & \Sigma = 0.027 \text{ cm}^2/\text{gm at 6 MeV,} \\ K = 0.68, & \rho = 1.74 \text{ gm/cm,} \\ A = 60 \text{ gm/gm.mole,} & N_2 = 2 \text{ atoms/molecule,} \end{array}$$

$$\phi_{i2} = 3.73 \times 10^3 \frac{V_i}{r_i^2 R_i^2} \exp \left[ -0.05 \ell_i - 0.047 S_i \right]. \quad (B-5)$$

The evaluation of equation (B-5) for each segment results in the conclusion that 83 percent of the oxygen activation gamma rays that reach the detector position originate in the top 10 cm of the sample and 11 percent originate in the layer 10 to 20 cm below the surface. If Zones S and D (see Figure B-1) are once more considered and are again defined as being 20 cm thick, it is found that Zone D contributes 43 percent while Zone S contributes only 32 percent. Thus the active volume of the sample for the  $O^{16}(n,p)N^{16}$  reaction tends also to be concentrated towards the detector.

For the geometry just considered, i.e., a large  $SiO_2$  sample with the neutron source located 15 cm above the surface and the detector located 15 cm above the surface and 40 cm from the neutron source, the active volumes for the capture gamma rays and for the oxygen activation gamma rays essentially coincide. The ratio of the number of silicon capture gamma rays to the number of oxygen activation gamma rays striking the crystal is 0.11. Hence, the oxygen activation gamma rays will dominate the spectrum.

#### Source 5 cm Above Surface

On the basis of the measured thermal neutron flux distribution reported in Figure B-2, calculations were performed to determine the active volume for both thermal neutron capture and fast activation of oxygen for the following detector positions: (a) directly above the neutron source, 40 cm above the surface, (b) directly above the neutron source, 50 cm above the surface, (c) 5 cm above the surface, 30 cm from the neutron source, and (d) 5 cm above the surface, 40 cm from the neutron source. In cases (a) and (b) the sample

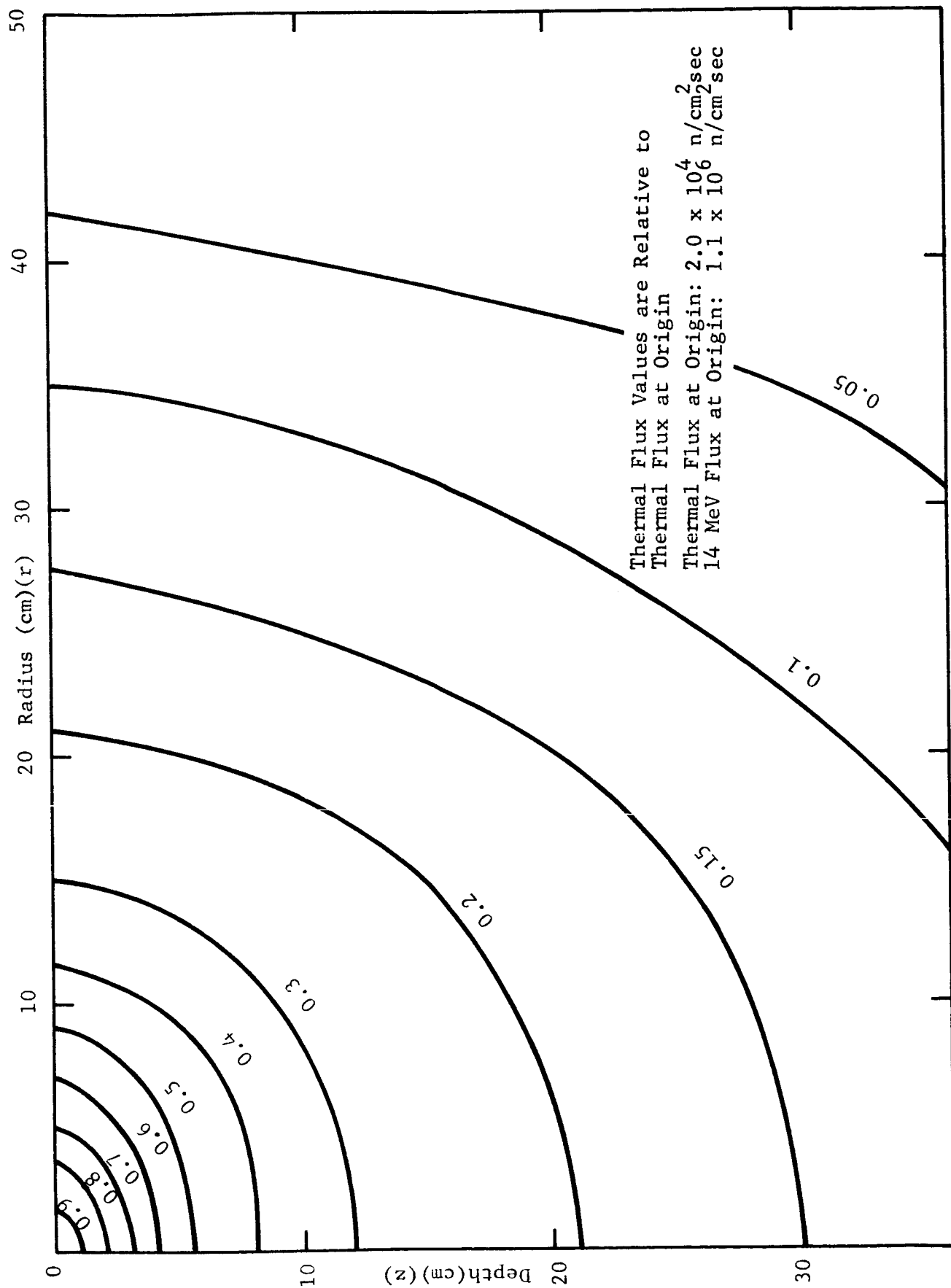


Figure B-2  
CONTOUR PLOT OF THE THERMAL NEUTRON FLUX DISTRIBUTION IN IRON-SAND SAMPLE WITH 4cm OF REFLECTOR  
ABOVE THE NEUTRON SOURCE AND SOURCE 5cm ABOVE THE SAMPLE

was divided into 29 segments, and in cases (c) and (d) the sample was divided into 128 segments. Equation (B-2) was used for the thermal neutron capture in silicon and equation (B-5), modified for the 14-MeV flux of  $1.1 \times 10^6 \text{ n/cm}^2 \text{ sec}$  at the surface, was used for the oxygen activation.

The results of the calculations. listed in Table B-1, indicate that, for all four detector geometries, about 60 percent of the capture gamma rays and about 75 percent of the oxygen activation gamma rays which reach the detector originate in the top 8 cm of the sample.

Let Zone S' be a volume of sample enclosed by a cylinder having a 20 cm radius and a 15 cm thickness and centered directly below the neutron source, and let Zone D' be a volume of sample identical to that of Zone S' but centered 10 cm from a point directly below the detector position and in the direction of the source. For detector geometry (c) the calculations show that Zone S' contributes 29 percent of the total capture gamma-ray flux while Zone D' contributes 62 percent and Zone S' contributes 50 percent of the total activation gamma-ray flux while Zone D' contributes 68 percent. For detector position (d) Zone S' contributes 16 percent and Zone D' contributes 55 percent of the capture gamma-ray flux; Zone S' contributes 36 percent and Zone D' contributes 55 percent of the activation gamma-ray flux.

The above results indicate that, if the detector is located in a horizontal geometry (i.e., the same height above the sample as the neutron source), shielding of the detector from the region of the sample directly below the neutron source (i.e., Zone S') will improve somewhat the ratio of capture to activation gamma rays. The calculated ratios of silicon capture gamma rays to oxygen activation gamma rays for the four detector positions are 0.073 for detector position (a), 0.082 for (b), 0.079 for (c), and 0.094 for (d). Thus, if the gamma rays originating in region S' could be

Table B-1

ORIGIN OF GAMMA RAYS REACHING THE DETECTOR  
WITH SOURCE 5 cm ABOVE SURFACE

Detector Position	Layer	Percent of Gamma Rays Incident on Detector	
		Capture	Activation
(a)	0-2 cm	24	39
	2-8 cm	38	41
	8-20 cm	29	18
	> 20 cm	9	2
(b)	0-2 cm	22	39
	2-8 cm	37	43
	8-20 cm	30	16
	> 20 cm	11	2
(c)	0-5 cm	53	73
	5-15 cm	32	23
	15-30 cm	11	4
	30-50 cm	4	---
(d)	0-5 cm	54	74
	5-15 cm	33	23
	15-30 cm	10	3
	30-50 cm	3	---

eliminated, the ratios would increase to 0.11 for detector position (c) and 0.12 for detector position (d).

The ratios of iron capture gamma rays to oxygen activation gamma rays were calculated for iron-sand-sample 2 and detector positions (a), (b), and (c). The results are 0.21 for detector position (a)(the measured value with a detector 37 cm above the sample was 0.15), 0.084 for detector position (b)(the measured value with a detector 52 cm above the sample was 0.087), and 0.28 for detector position (c)(the measured value with a detector 37 cm from the target and 5 cm above the sample was 0.31). This agreement between the calculated and experimental results is considered to be quite good.

APPENDIX C  
SAMPLE OF DIGITAL DATA

Digital Data for Figure 27

Capture Gamma-Ray Spectrum of Iron-Sand Sample Obtained Using  
 Sandia Geometry With 4 cm Paraffin Above Target

0	000000	052050	951973	801855	161590	168595	153797	130241
8	106396	086960	072511	062882	053278	047888	049893	061817
16	042429	029612	028111	026342	025765	024434	023070	022841
24	024610	022552	019732	018848	018644	017991	017012	015253
32	015914	015347	015209	015459	015184	014283	013269	012911
40	012701	012408	011155	009701	008870	008003	007354	007807
48	011523	016389	014890	008609	005175	004121	003676	003470
56	003202	003205	003179	003134	003315	003300	003227	002908
64	002680	002532	002578	002541	002518	002488	002481	002510
72	002396	002339	002341	002442	002417	002389	002317	002238
80	002177	002037	002198	002171	002149	002056	002162	001974
88	002086	001940	001919	001842	001969	001845	001785	001786
96	001859	001943	001847	001735	001728	001624	001596	001565
104	001638	001565	001524	001508	001556	001498	001405	001387
112	001365	001363	001335	001343	001396	001294	001321	001411
120	001447	001421	001437	001339	001239	001286	001239	001191
128	001208	001135	001150	001152	001266	001264	001290	001375
136	001458	001421	001496	001580	001512	001395	001378	001370
144	001374	001323	001320	001288	001294	001255	001391	001584
152	001765	001853	001759	001516	001417	001231	001199	001138
160	001121	001083	001001	000982	001016	001138	001298	001338
168	001253	001168	000893	000826	000744	000771	000691	000652
176	000696	000665	000725	000790	000745	000759	000739	000679
184	000727	000698	000660	000619	000632	000570	000589	000584
192	000648	000786	000865	000766	000705	000599	000576	000492
200	000424	000406	000376	000328	000278	000266	000317	000366
208	000381	000405	000333	000266	000246	000157	000169	000131
216	000137	000119	000124	000104	000102	000076	000079	000076
224	000074	000069	000069	000083	000060	000058	000080	000072
232	000075	000074	000059	000066	000045	000073	000037	000073
240	000066	000065	000071	000054	000050	000050	000052	000047
248	000045	000048	000044	000034	000031	000036	000034	000036

1287050

# Digital Data for Figure 29

Capture Gamma-Ray Spectrum of Iron-Sand Sample Obtained Using  
Sandia Geometry With 4 cm Boronated Paraffin Above Target

0	000000	079353	618336	042842	176416	186975	169867	147003
8	119363	096408	080578	069499	060348	054772	055751	066123
16	048365	034522	032913	031131	029582	028393	026866	026692
24	030677	028543	023266	021805	021499	020590	019610	018702
32	018179	017475	017476	017475	017477	016269	015202	014518
40	014286	013569	012834	010966	009745	008945	008276	008153
48	011783	017425	016596	010038	006017	004601	004116	003920
56	003627	003558	003598	003518	003526	003530	003407	003267
64	003000	002800	002836	002738	002761	002870	002657	002600
72	002600	002649	002599	002655	002667	002631	002353	002373
80	002274	002185	002300	002205	002330	002213	002167	002135
88	002110	002094	002020	002000	001963	001995	001879	001866
96	001903	001873	001876	001765	001731	001777	001629	001622
104	001535	001662	001649	001532	001623	001464	001417	001430
112	001350	001347	001372	001342	001383	001235	001353	001331
120	001374	001446	001294	001301	001294	001242	001328	001206
128	001157	001149	001127	001213	001198	001194	001235	001321
136	001385	001430	001543	001505	001489	001376	001345	001371
144	001332	001337	001319	001346	001293	001249	001322	001573
152	001828	001818	001929	001646	001450	001278	001221	001165
160	001111	001042	000892	000928	001032	001077	001233	001328
168	001287	001126	000934	000770	000724	000741	000687	000626
176	000605	000594	000639	000645	000626	000613	000604	000603
184	000573	000511	000512	000543	000477	000473	000417	000469
192	000483	000549	000572	000545	000545	000483	000391	000345
200	000345	000332	000285	000255	000251	000228	000231	000252
208	000270	000257	000249	000238	000182	000153	000150	000131
216	000134	000118	000116	000106	000109	000094	000098	000091
224	000078	000089	000062	000075	000074	000084	000077	000067
232	000075	000092	000063	000067	000067	000063	000068	000074
240	000059	000074	000064	000071	000054	000058	000056	000049
248	000060	000047	000039	000036	000044	000030	000039	000039

1287090